Mechanisms of selenium removal by partially oxidized magnetite nanoparticles for wastewater remediation

Nicolas Börsig [a,*], Andreas C. Scheinost [b,c], Dieter Schild [d], Thomas Neumann [e]

[a] Karlsruhe Institute of Technology (KIT), Institute of Applied Geosciences, Adenauerring 20b, 76131, Karlsruhe, Germany
[b] Helmholtz-Zentrum Dresden-Rossendorf (HZDR), Institute of Resource Ecology, Bautzner Landstraße 400, 01328, Dresden, Germany
[c] The Rossendorf Beamline (ROBL) at ESRF, 38043, Grenoble, France
[d] Karlsruhe Institute of Technology (KIT), Institute for Nuclear Waste Disposal, Hermann-von-Helmholtz-Platz 1, 76344, Eggenstein-Leopoldshafen, Germany
[e] Technische Universitat Berlin, Institute of Applied Geosciences, Ernst-Reuter-Platz 1, 10587, Berlin, Germany

ABSTRACT

Magnetite nanoparticles are a promising cost-effective material for the remediation of polluted wastewaters. Due to their magnetic properties and their high adsorption and reduction potential, they are particularly suitable for the decontamination of oxyanion-forming contaminants, including the highly mobile selenium oxyanions selenite and selenate. However, little is known how the remediation efficiency of magnetite nanoparticles in field applications is affected by partial oxidation and the formation of magnetite/maghemite phases. Here we characterize the retention mechanisms and capacity of partially oxidized nanoparticulate magnetite for selenite and selenate in an oxic system at different pH conditions and ionic strengths. Data from adsorption experiments showed that retention of selenate is extremely limited except for acidic conditions and strongly influenced by competing chloride anions, indicating outer-sphere adsorption. By contrast, although selenite adsorption capacity of oxidized magnetite is also adversely affected by increasing pH, considerable selenite quantities are retained even at alkaline conditions. Using spectroscopic analyses (XPS, XAFS), both mononuclear edge-sharing (^{2}E) and binuclear corner-sharing (^{2}C) inner-sphere selenite surface complexes were detected, while reduction to Se(0) or Se(–II) species could be excluded. Under favourable adsorption conditions, up to ~pH 8, the affinity of selenite to form ^{2}C surface complexes is higher, whereas at alkaline pH values and less favourable adsorption conditions ^{2}E complexes become more dominant. Our results demonstrate that magnetite can be used as a suitable reactant for the immobilization of selenite in remediation applications, even under (sub)oxic conditions and without the involvement of reduction processes.

1. Introduction

Selenium (Se) pollution of soils, sediments and waters is a global phenomenon. Although Se is a naturally occurring trace element, the major cause of Se release and contamination are human activities such as coal production and combustion, phosphate and sulphide-ore mining, metal processing, oil refining, waste disposal or agricultural irrigation (Dhillon and Dhillon, 2003; Lemly, 2004; Tan et al., 2016). Additionally, Se occurs in vitrified high-level nuclear waste (HLW) in the form of the long-lived, harmful radionuclide ^{79}Se and plays a major role in the long-term safety assessment of HLW repositories (Bingham et al., 2011; De Cannière et al., 2010; Frechou et al., 2007).

In aquatic systems, Se levels can rapidly become toxic endangering not only the health of aquatic organisms but also of other beings, including humans, due to bioaccumulation in the food chain (Lenz and Lens, 2009; Munier-Lamy et al., 2007). Mobility and bioavailability of Se in water is mainly controlled by its solubility and retention through biogeochemical processes (Dhillon and Dhillon, 2003; Fernández-Martínez and Charlet, 2009), which are largely determined by the prevailing Se oxidation state and speciation (Fig. 1a). Under reducing conditions, Se forms sparingly soluble minerals and compounds, primarily elemental selenium (Se^0) and metal selenides (Se(–I) and Se(–II)) (Fig. S1). Under (sub)oxic conditions, however, inorganic Se occurs in the oxidation state Se(IV) and Se(VI) as highly soluble and mobile oxyanions selenite (SeO$_3^{2-}$) and selenate (SeO$_4^{2-}$). Both selenite and selenate can appear in protonated or deprotonated form, depending on the

solution pH (Fig. 1b).

A key factor controlling the fate of dissolved Se oxyanions in aquatic environments is sorption on geological materials. Of special relevance in this context are metal (hydr)oxides and particularly iron (hydr)oxides due to their high affinity towards oxyanion-forming pollutants such as Se, As, Sb, V, Mo or Cr (Borsig et al., 2017; Chan et al., 2009; Nakamaru and Altansuvd, 2014; Weidner and Ciesielczyk, 2019). Besides adsorption, reduction of oxyanions to less soluble compounds is an important abiotic immobilization process (Kirsch et al., 2008; Scheinost et al., 2008; Wilkin et al., 2005), driven by Fe^0 or by Fe(II)-bearing iron (hydr) oxides, yet depends strongly on the prevailing redox conditions.

Magnetite [Fe_3O_4] is one of the most widespread iron (hydr)oxide minerals in nature and is also known as a sink for dissolved oxyanions due to its high adsorption and reduction potential. Due to these properties and its magnetic character, the use of magnetite is considered in various *in situ* and *ex situ* environmental remediation approaches, including wastewater treatment or soil remediation (Kuppusamy et al., 2016; Usman et al., 2018). Particularly for decontamination of wastewaters based on removal of hazardous oxyanions by nanoremediation, nanoparticulate magnetite is a promising cost-effective material (Chowdhury and Yanful, 2010; Horst et al., 2015; Li et al., 2017), as shown by several previous studies (Jordan et al., 2009; Loyo et al., 2008; Martínez et al., 2006; Missana et al., 2009; Scheinost and Charlet, 2008; Usman et al., 2018).

For field applications, however, it must be taken into account that reactivity and capacity of a remediation material is highly dependent on its stability under various environmental conditions. This applies in particularly for redox- and pH-sensitive minerals such as magnetite and other reduced or mixed-valent iron minerals like zerovalent iron (ZVI) and green rust (Borsig et al., 2018; Génin et al., 2006; Liu et al., 2014; Mu et al., 2017). A common phenomenon for magnetite is thereby the transformation into maghemite [γ-Fe_2O_3] in (sub)oxic environments (Fig. S1) due to partial or complete oxidation (Iyengar et al., 2014; Li et al., 2019; Rebodos and Vikesland, 2010).

$$4\, Fe^{II}Fe_2^{III}O_4 \; + \; O_2 \rightarrow 6\, \gamma\text{-}Fe_2^{III}O_3$$
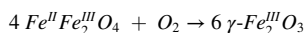
Maghemite is the Fe(II)-free oxidation product of magnetite and since it has the same spinel crystal structure as magnetite, both minerals represent the end members of a solid solution series (Gorski and Scherer, 2010; Iwatsuki and Fukasawa, 1993). Oxidation of magnetite generally results in the formation of a maghemite surface layer. However, while this maghemite layer can protect the bulk of the underlying magnetite from further oxidation for larger sized (non-nano) particles,

nanoparticulate magnetite is more vulnerable to oxidation (He and Traina, 2005; Khan et al., 2015; Rebodos and Vikesland, 2010). In this case, oxidation can lead to significant amounts of maghemite in the near-surface region (core-shell structure) or even to complete transformation (Kuhn et al., 2002; Sharifi Dehsari et al., 2018; Signorini et al., 2003).

In order to assess the efficiency of magnetite for remediation measures, it is therefore important to know to what extent oxidation and formation of a mixed magnetite/maghemite phase (non-stoichiometric magnetite) affects the retention of pollutants in (sub)oxic systems, particularly in terms of the specific mechanisms. The aim of this paper was therefore to characterize the retention efficiency of partially oxidized magnetite with respect to dissolved Se oxyanions under oxic conditions. Although a respectable number of studies have dealt with the capacity of Se oxyanion retention by magnetite in the context of wastewater treatment or HLW disposal (Gonzalez et al., 2010; Jordan et al., 2009; S. S. Kim et al., 2012; Martínez et al., 2006; Verbinnen et al., 2013; Wei et al., 2012), studies investigating the sorption mechanisms at the molecular level are rather rare (Loyo et al., 2008; Missana et al., 2009). Besides, there is to our knowledge no publication dealing with the retention of selenium oxyanions specifically on partially oxidized magnetite nanoparticles as they would occur in (sub)oxic wastewater treatment applications. In this study, we examined the interaction of selenite and selenate with pre-oxidized magnetite in adsorption experiments at various hydrochemical conditions, including pH and ionic strength. By using hydrochemical data and a combination of solids analyses, we were able to determine the Se retention capacity and stability as well as the involved immobilization mechanisms.

2. Materials and methods

2.1. Synthesis of magnetite

Magnetite (Mt) was synthesized in the laboratory by progressively oxidizing an aqueous Fe^{2+} solution under alkaline pH conditions (Fig. S2). A detailed description of the synthesis procedure, sample preparation, and characterization of the final product can be found in Borsig et al. (2018). In short, 5 g $FeCl_2 \cdot 4H_2O$ were dissolved in 500 ml N_2-degassed Milli-Q water. After adding 55 mL 1 M KOH and 25 mL 1 M $NaHCO_3$ solution, the pH value of the solution increased and blueish green coloured iron(II) hydroxide precipitated (Table S1). Continuous stirring resulted in the progressive oxidation of the initial anoxic system by atmospheric oxygen, causing the transformation of iron(II) hydroxide
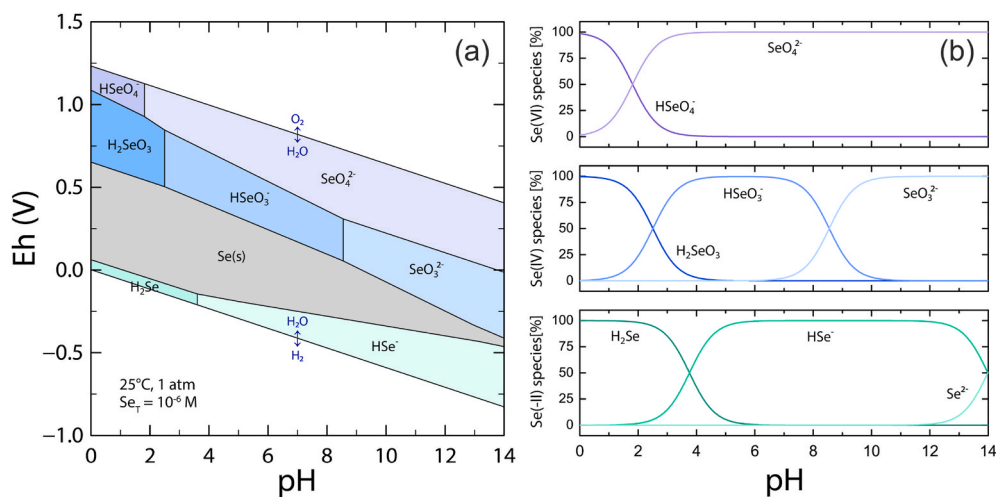
Fig. 1. (a) Eh-pH diagram for the system Se–H_2O at 25 °C and 1 atm; Se_{total}: 10⁻⁶ mol/L. (b) Stability and distribution of dissolved Se(–II), Se(VI), and Se(VI) species as a function of pH. Diagrams were calculated with PHREEQC (USGS) using an adapted *wateq4f* database; thermodynamic Se data: aquatic species from Séby et al. (2001), solid phases from Salah and Wang (2014).

into black magnetite within 48 h. With approximately 2 g of magnetite formed, the mass to volume ratio (m/V) during synthesis was about 3.4 g/L and the final pH was around 9.2. After synthesis, the magnetite phase was decanted, centrifuged and washed three times with Milli-Q water. After drying at 40 °C for 48 h, the synthesized particles were gently ground with an agate mortar to avoid altering the particle surfaces before they were stored for analysis and adsorption experiments.

2.2. Adsorption experiments

Adsorption of selenite and selenate on pre-oxidized magnetite was studied in batch experiments under oxic conditions. The experimental setup was almost identical to the conditions at the end of the magnetite synthesis. To investigate selenite and selenate adsorption as a function of the Se concentrations, 50 ml 0.01 M KCl solution that contained distinct volumes of Se stock solution was added to 170.0 mg of washed magnetite powder (m/V ratio   3.4 g/L). The Se stock solutions were prepared by dissolving defined quantities of Na_2SeO_3 or $Na_2SeO_4 \cdot 10H_2O$ in N_2-degassed Milli-Q water. The added volumes were calculated to obtain initial selenite or selenate concentrations of 10^{-5} - 10^{-2} mol/L. KCl was used as background electrolyte since also the original synthesis took place in such conditions and to simulate solutions with higher ionic strengths. After mixing, the pH was adjusted to 9.2 by dropwise addition of KOH solution. The 50 mL flasks were sealed and constantly shaken for 48 h to ensure that adsorption equilibrium was achieved (pre-study and comparable studies (Duc et al., 2003; Matulová et al., 2019; Su and Suarez, 2000) showed fast reaction kinetics with less than 1 h to reach equilibrium). Due to the strong buffering capacity of magnetite, pH was checked after 24 and 45 h and if necessary readjusted to pH 9.2. Afterwards, the residual Se concentration in solution was analysed and the solids were dried at 40 °C both with and without prior washing.

In addition, similar batch experiments were carried out to study the influence of pH and ionic strength. While selenite or selenate concentration was kept constant (10^{-4} mol/L), different ionic strengths of 0.01 M KCl or 0.14 M KCl were tested and pH values were adjusted in the range of 2–14 using either HCl or KOH solution.

2.3. Analytical techniques

Dissolved Se and Fe concentrations were determined by Inductively-Coupled Plasma Optical Emission Spectrometry (ICP-OES; Varian 715-ES) or Inductively-Coupled Plasma Mass Spectrometry (ICP-MS; X-Series 2, Thermo Fisher Scientific Inc.) depending on the solution concentrations. X-Ray Diffraction (XRD) for analysis of the phase composition was performed on a Bruker D8 Advance X-ray diffractometer (Cu Kα). The total Se content of solid phases was determined by polarized Energy Dispersive X-ray Fluorescence Spectroscopy (pEDXRF) with an Epsilon 5 (PANalytical). Electron microscopy with Energy Dispersive X-ray Spectroscopy (EDX) was used to characterize the solid phases. Images were recorded using a LEO 1530 (Zeiss Inc.) Scanning Electron Microscope (SEM) with a NORAN System SIX (Thermo Electron Corp.) EDX-System. To examine oxidation states and to identify elemental composition of the surface area, X-ray Photoelectron Spectroscopy (XPS) measurements were performed using a PHI 5000 VersaProbe II (ULVAC-PHI, Inc.). Detailed information about measurement parameters, sample preparation, and data evaluation are described in the supplementary data (SD).

X-ray absorption spectroscopy was carried out on selected samples to identify the Se oxidation state, coordination as well as the molecular short-range structure. Se K-edge X-ray Absorption Fine Structure (XAFS) spectra were collected at the Rossendorf Beamline (ROBL) at ESRF (Grenoble, France). Measurement parameters and sample preparation are described in detail in the SD. Fluorescence deadtime correction, energy calibration and averaging of scans was performed with the software package SixPack (www.sams-xrays.com/sixpack), while

normalization and extraction of the EXAFS chi function was performed with the software WinXAS according to standard procedures (Ressler, 1998). The k^3-weighted EXAFS data were fit using theoretical back-scattering amplitudes and phase shifts calculated with FEFF 8.2 (Ankudinov and Rehr, 1997). Statistical analysis of spectra was performed with the ITFA program package (Rossberg et al., 2003). Spectra of Se reference samples were taken from Scheinost and Charlet (2008).

3. Results and discussion

3.1. Characterization of synthesized magnetite

XRD analysis of the synthesis product proved the formation of magnetite [Fe_3O_4] without evidence for the presence of maghemite according to Kim et al. (2012) or other additional phases. According to SEM characterization, the magnetite consisted of aggregated particles with an individual particle size of about 50 nm. A specific surface area of 32 m^2/g was determined by BET analysis, consistent with literature values (Cornell and Schwertmann, 2003; Salazar Camacho and Villalobos Penalosa, 2017). XPS analysis and evaluation of the Fe $2p_{3/2}$ spectra after Huber et al. (2012), however, showed that the Fe(II) to Fe$_{total}$ ratio was only 0.14 (±5 % standard deviation) at the surface and therefore lower than the expected ratio of 0.33 for stoichiometric Fe_3O_4. Note that the information depth of the Fe $2p_{3/2}$ elemental line of magnetite was calculated with 2.2 nm (see SD). This indicated that the synthesized magnetite was partially oxidized and that the near-surface region of the particles consists of both magnetite and maghemite.

3.2. Selenium adsorption capacity of partially oxidized magnetite

Fig. 2a shows the adsorption capacity of partially oxidized magnetite for selenite and selenate under oxic conditions as a function of pH and ionic strength. The results demonstrate that the adsorption behaviour is primarily affected by the Se species. Selenate is only immobilized under extreme acidic conditions and even the data points for pH 2 are in the range of the adsorption edge. Contrary to selenate, the entire initial selenite amount is immobilized at low pH (<pH 5) and the adsorption edge extends over a wide pH range from weakly acidic to alkaline (pH 6–11) conditions. Furthermore, while the adsorption edge of selenate shifts towards lower pH values (~1.5 pH unit) in the presence of higher KCl concentrations, retention of selenite is not affected by higher ionic strengths. The analysis of the residual Fe and Se concentration as a function of solution pH (Fig. S3) further showed significantly increasing Fe concentrations at <pH 4, indicating incipient dissolution of magnetite at low pH values. The Se retention behaviour is however not affected by this process due to the high positive surface charge of the remaining magnetite at acidic conditions. Moreover, the impact of ionic strength can also be seen in Fig. 2b, which shows the distribution coefficient (K_d) as a function of the selenite equilibrium concentration at pH 9.2. With increasing concentrations of dissolved Se, log K_d values decrease steadily but are identical for both ionic strengths. The absolute K_d values are furthermore quite high (log K_d: 3.2–1.2 L/kg) and correspond to Se surface coverages in the range of 0.05–2.5 at/nm^2. Unlike selenite, adsorption of selenate was too low to obtain reliable K_d data at pH 9.2.

The observed adsorption behaviour is consistent with the literature. Adsorption capacities of iron (hydr)oxides for anions such as selenite and selenate decrease with increasing pH as the amount of positively charged surface groups declines by deprotonation. Since in particular the single-protonated Se species ($HSeO_3^-$ and $HSeO_4^-$) interact with the hydroxyl groups on the iron (hydr)oxide surface (Kim et al., 2012; Martínez et al., 2006), the position of the adsorption edges also correlates with the pH-dependent distribution of those species in solution (Fig. 1). However, even at alkaline conditions of >pH 10, where the particle surface is negatively charged, considerable amounts of selenite are adsorbed. (Although actual PZC values generally depend on
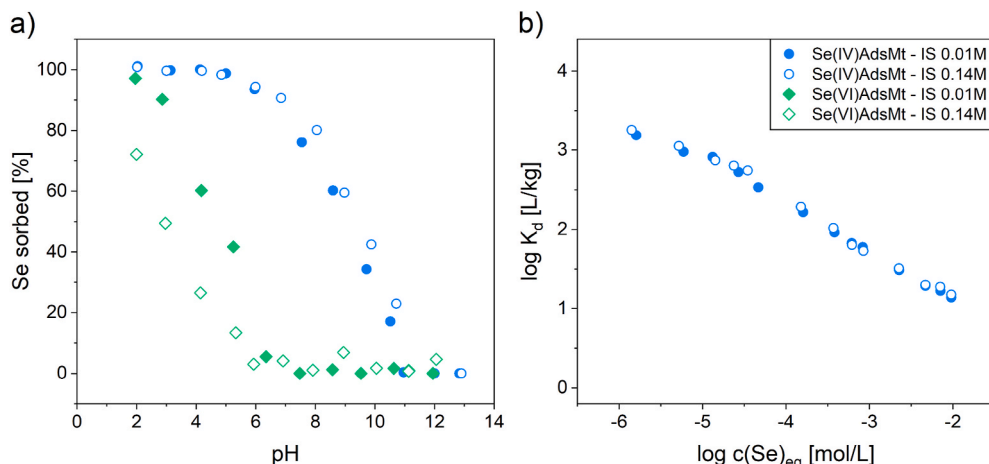
Fig. 2. (a) Selenite and selenate adsorption on magnetite (Mt) depending on pH and ionic strength (IS) at initial Se concentrations of 10^{-4} mol/L. (b) Uptake of selenite by magnetite at pH 9.2 as a function of the Se equilibrium concentration.

numerous factors such as particle size, ionic strength, adsorption of ions, or the presence of coatings, the reported PZC values by Hu et al. (2010), Kosmulski (2020), and Milonjić et al. (1983) for both magnetite and maghemite range maximally to ~pH 8.1). Responsible for this immobilization is the specific adsorption of selenite resulting in the formation of inner-sphere surface complexes (Jordan et al., 2009; Kim et al., 2012; Loyo et al., 2008; Martínez et al., 2006). Due to this inner-sphere selenite adsorption, large distribution coefficients as well as high Se surface coverages of up to 2.5 at/nm^2 can be observed even at pH 9.2. Such values were found not only for magnetite (Kim et al., 2012) but also for hematite and goethite (Borsig et al., 2017; Duc et al., 2003; Rovira et al., 2008; Su and Suarez, 2000). In addition, formation of inner-sphere complexes explains why selenite adsorption is not dependent on the ionic strength. By contrast, selenate primarily forms outer-sphere adsorption complexes in contact with iron (hydr)oxides (Hayes et al., 1987; Jordan et al., 2013; Rietra et al., 2001). This would explain the almost non-existent adsorption at higher pH values as well as the negative impact of higher ionic strengths as both parameters cause unfavourable adsorption conditions due to decreasing positive surface charges and competition effects.

When interpreting these adsorption data, it must be taken into account that the used magnetite phase was partly oxidized to maghemite in its near-surface region under the prevailing oxic conditions. However, the comparison of Se adsorption studies on magnetite and maghemite reveals that both minerals behave very much alike. The adsorption capacity of both maghemite and magnetite is similar in terms of its dependence on Se speciation, pH or ionic strength (Jordan et al, 2013, 2014). Also maghemite exhibits fast Se adsorption kinetics, with Se(IV) adsorption occurring at neutral and even alkaline conditions, whereas adsorption of Se(VI) is limited to <pH 7. Moreover, while Se(IV) adsorption is not affected by ionic strength, higher background electrolyte concentrations result in decreased adsorption and a shift of the adsorption edge (1–2 pH units) for Se(VI). Interesting is also that several previous Se adsorption studies on magnetite led to similar results regardless of whether the experiments were performed under oxic (Martínez et al., 2006) or anoxic conditions (Jordan et al., 2009; Kim et al., 2012; Loyo et al., 2008). In comparative studies Missana et al. (2009) proved that no differences in terms of selenite sorption occurred under oxic and anoxic conditions. Furthermore, it is not always documented to what extent the synthesized, industrially-produced or natural magnetite tested in the above-mentioned sorption studies might also have been affected by a partial oxidation into maghemite. In contrast, magnetite synthesized under well controlled, anoxic conditions proved to be a very effective reducer for selenite (Scheinost et al., 2008; Scheinost and Charlet, 2008).

3.3. Effects of selenium adsorption on the properties of the solid phase

To assess the impact of selenite or selenate adsorption on the properties of the magnetite phase, selected samples from adsorption experiments were characterized by various solids analysis methods. A detailed description and evaluation of these analyses can be found in the SD Chapter 3.2. In short, XRD and SEM/EDX analyses demonstrated that neither the mineralogical composition (Fig. S4) nor the morphology (Fig. S5) of the initial magnetite nanoparticles was affected by the adsorption of selenite or selenate. EDXRF data (Table S2) and SEM/EDX analysis (Fig. S5), however, proved that the examined solid samples contained significant Se quantities after adsorption, whose proportions depend on the initial Se speciation and concentration. For a solid sample from the selenite system, with a relatively high total Se amount of 4200 ppm, the oxidation state of this Se proportion was identified by XPS as Se(IV) (Table S3), demonstrating that retention of selenite is not accompanied by a redox change.

Furthermore, XPS analysis and the comparison of the Fe(II)/Fe$_{total}$ ratio of solids before and after adsorption of selenite or selenate yielded comparable results (Table S3). The observation that the oxidation of magnetite to maghemite is not progressing significantly during the oxic adsorption experiments can be explained by the formation of an initial maghemite oxidation layer that slows down aerial oxidation of the underlying magnetite core (He and Traina, 2005; Khan et al., 2015; Rebodos and Vikesland, 2010).

3.4. Characterization of the adsorption complexes

Se K-edge XAFS analysis was used to characterize the oxidation state (XANES) as well as the local structure (EXAFS) of the immobilized Se. For this purpose, magnetite samples from selenite or selenate adsorption experiments conducted at pH 4, 7, and 9.2 were analysed in order to investigate the influence of pH on the sorption mechanism.

Unfortunately, even at pH 4, selenate sorption on magnetite was too low to be analysed by XAFS spectroscopy. A determination of the specific adsorption mechanisms was therefore not possible in case of the selenate system. Generally, the low selenate retention capacity in combination with the negative impact of higher ionic strengths and pH values generally points to the formation of outer-sphere adsorption complexes. That selenate oxyanions form primarily outer-sphere complexes in contact to iron (hydr)oxides was previously shown for maghemite (Jordan et al., 2013) and hematite (Borsig et al., 2017) by XAFS, as well as by SCM for magnetite (Martínez et al., 2006). It should be noted, however, that the observed dependency on ionic strength and pH alone is not an unambiguous characteristic in favour of an

outer-sphere selenate adsorption (Su and Suarez, 2000).

Unlike the samples from the selenate systems, the selenite samples had taken up enough Se to be analysed by XAFS analysis. Fig. 3 shows the Se K-edge XANES spectra of the analysed samples from the selenite system together with reference spectra of Se(IV) (Na_2SeO_3 solution) and Se(0) (grey elemental Se) compounds. For all three samples, the adsorption edge exactly matches that of the Se(IV) reference spectra (12.660 keV), indicating that the initial tetravalent oxidation state remained unchanged. Furthermore, a statistical analysis of the spectra using the ITFA software package (Rossberg et al., 2003) showed that the three sample spectra contained only one spectral component commensurate with Se(IV), and not with any other Se oxidation state tested (Se (VI), Se(0), Se(–II)). Hence, contributions from these latter oxidation states are smaller than 5 % (Charlet et al., 2007). XANES data are thus in line with the XPS results which showed that the adsorption processes caused neither selenite reduction nor oxidation. An immobilization due to selenite reduction and formation of sparingly soluble reduced Se compounds such as elemental Se^0 or selenide minerals can therefore be excluded not only at alkaline but also at acidic pH conditions. It is
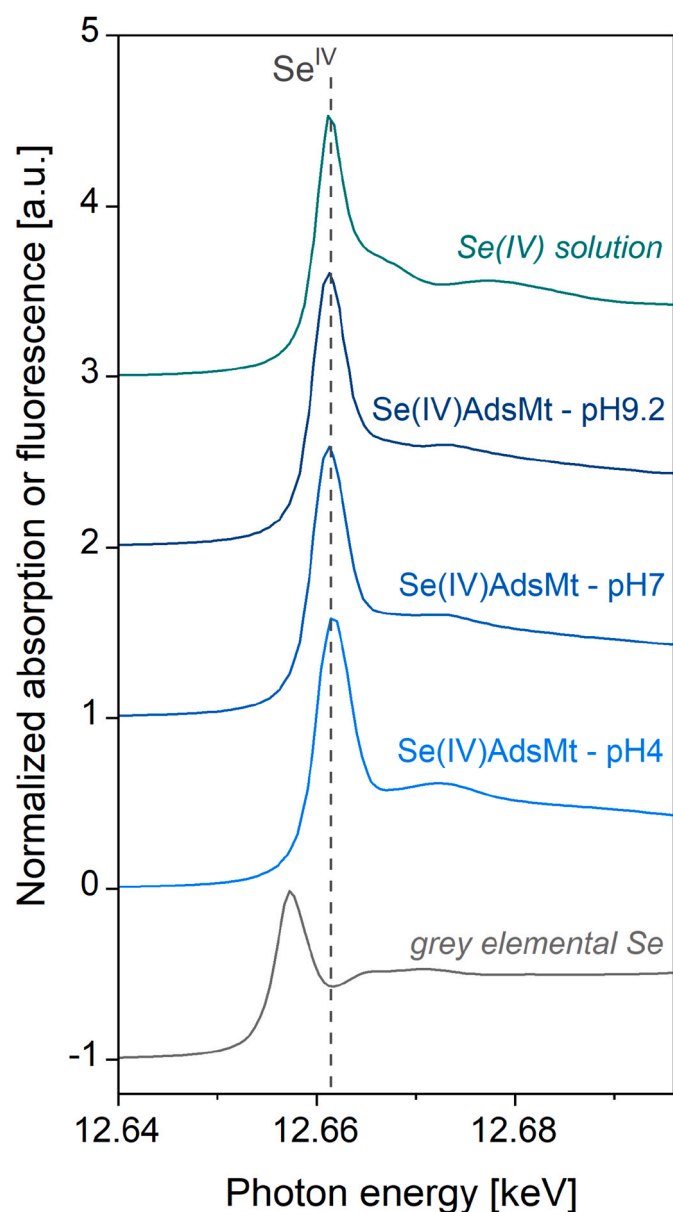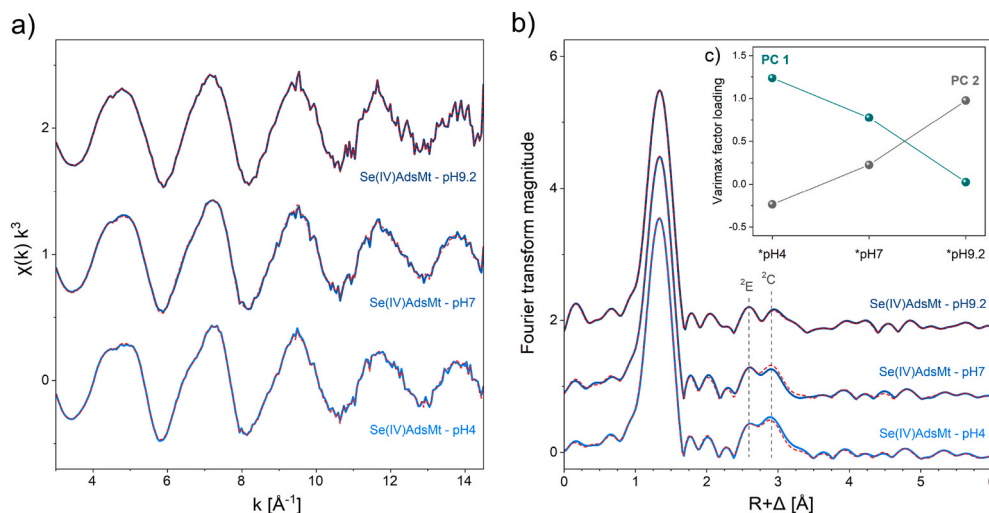
known that in anoxic systems reduction of selenite oxanions by Fe (II)-bearing minerals like magnetite is generally possible (Borsig et al., 2018; Scheinost et al., 2008; Scheinost and Charlet, 2008). However, even in an anoxic environment, selenite reduction does not inevitably take place, as other selenite-magnetite adsorption studies have proven (Jordan et al., 2009; Loyo et al., 2008; Missana et al., 2009). The exact reasons for this are unclear, but several possible explanations have been discussed in previous studies. According to Loyo et al. (2008), one reason could be the slow reaction time of the selenite reduction process. However, a direct comparison of the reaction times used in the above-mentioned studies, ranging from a few hours to 30 days, is difficult because of the partially different experimental setups (i.e. initial Se concentrations, magnetite amounts, pH, presence of secondary ions, etc.). For this reason, the reaction time must rather be seen in relation to the respective mineral surface coverage and reduction kinetics. According to Missana et al. (2009), reduction of selenite oxanions is only possible if the selenite surface coverage of the corresponding Fe (II)-bearing mineral phase is relatively low, as high coverages slow down electron transfer processes. This theory, however, has not yet been experimentally proven. Furthermore, the presence or absence of Se reduction processes could be affected by the specific Fe(II)/Fe(III) ratio of the magnetite phase, since the magnetite stoichiometry strongly influences its physicochemical properties, including sorption capacity and reduction potential (Gorski and Scherer, 2010). Higher Fe(II) fractions have a positive impact on the reduction potential of magnetite, which was proven in sorption studies with uranium (Latta et al., 2012) and neptunium (Wylie et al., 2016), among others.

To identify the specific adsorption type, the samples were analysed by Se K-edge EXAFS spectroscopy (Fig. 4a and b). The k^3-weighted spectra were fit with a FEFF 8.2 file generated with the crystallographic structure of mandarinoite ($Fe_2(SeO_3)_3 \cdot 6H_2O$, CIF 0005198, Hawthorne (1984)). For all three selenite sorption samples, the phase shift uncorrected EXAFS Fourier transforms (FT) are dominated by a strong peak at 1.35 Å. Responsible for this peak is the oxygen coordination shell. The fit of this shell using a single scattering Se–O path resulted in coordination number (CN) of 2.8 and atomic distances of 1.70–1.71 Å (Table 1), consistent with the tetravalent oxidation state and the unchanged pyramidal-shaped molecular structure of the selenite oxanion. Beyond the oxygen coordination shell, a small double peak arises in the range 2.3–3.5 Å, with the relative ratio of the two peaks changing with pH: for the sample representing acidic conditions [Se(IV)AdsMt-pH4], the right-side peak at 2.9 Å dominates, whereas under alkaline conditions [Se(IV)AdsMt-pH9.2] the left-side peak at 2.6 Å becomes more pronounced. In addition, the peak intensities at alkaline pH are generally lower than for acidic conditions. The peaks could be fitted with two individual single scattering Se–Fe paths, providing between 0.3 and 0.9 Fe atoms at an atomic distance of 2.90–2.93 Å, and 0.4–0.9 Fe atoms at an atomic distance of 3.37–3.40 Å (Table 1). Note that the Debye-Waller factors of both Se–Fe paths were kept correlated, to achieve satisfactory fitting of those peaks as well as to minimize the number of unknown parameters. The graphical representation of the fit results can be found in Fig. S6.

Although the necessity for such relatively small coordination numbers may be questioned at first due to their inevitably larger error, the use of two scattering paths was required to achieve stable fitting results. Contrary to this, the use of only one Se–Fe path or a mixture of Se–Fe and Se–O paths led to poor fitting results (Fig. S7). Furthermore, data of other studies (Jordan et al., 2014; Missana et al., 2009) as well as the results of principal component analysis (see Chapter 3.5) support this assumption.

The occurrence of Fe atoms in the second shell indicate an inner-sphere bonding between the selenite oxanion and the mineral surface. The shorter Fe shell with a distance of 2.90–2.93 Å points to the formation of a bidentate mononuclear edge-sharing ^2E arrangement. As shown in Fig. 5a, ^2E adsorption complexes are characterized by two oxygen atoms of the selenite molecule simultaneously forming the edge

Fig. 3. Se K-edge XANES spectra of Se references and magnetite samples from selenite adsorption studies performed at different pH; $c(Se)_0$: 10^{-3} mol/L.

Fig. 4. (a, b) Se K-edge EXAFS spectra of magnetite samples from selenite adsorption studies performed at different pH values (blue lines) and their reconstruction by two factors (red lines). (c) Varimax loadings of the two factors. (For interpretation of the references to colour in this figure legend, the reader is referred to the Web version of this article.)

Table 1
Se–K XANES edge energies and EXAFS fit results of selenite-magnetite adsorption samples ($S_0^2 = 0.9$).

Sample	E_0 [keV]	Oxygen shell				Iron shells				ΔE_0 [eV]	χ_{res} [%]
		CN[b]		R [Å][c]	σ^2 [Å²][d]	CN		R [Å]	σ^2 [Å²]		
Se(IV)AdsMt-pH4	12.6600	2.8	O	1.70	0.0019	0.9	Fe	2.93	0.0093[a]	14.8	12.5
						1.7	Fe	3.40	0.0093[a]		
Se(IV)AdsMt-pH7	12.6595	2.8	O	1.70	0.0018	0.5	Fe	2.93	0.0048[a]	15.4	13.4
						0.6	Fe	3.39	0.0048[a]		
Se(IV)AdsMt-pH9	12.6596	2.8	O	1.71	0.0017	0.3	Fe	2.90	0.0030[a]	15.7	14.6
						0.4	Fe	3.37	0.0030[a]		

[a] correlated σ^2.
[b] CN: coordination number, error ±25 %.
[c] R: radial distance, error ±0.01 Å
[d] σ^2: Debye-Waller factor, error ±0.0005 Å².

of an FeO_6 octahedron on the iron (hydr)oxide surface. The longer Fe shell, on the other hand, represents bidentate binuclear corner-sharing [2]C adsorption complexes, where one adsorbed selenite molecule is attached to two FeO_6 octahedra (Fig. 5b). That interaction of selenite oxyanions with iron (hydr)oxides can cause the (simultaneous) formation of these types of inner-sphere adsorption complexes, was also demonstrated by several previous studies (Borsig et al., 2017; Hayes et al., 1987; Hiemstra et al., 2007; Jordan et al., 2014; Kalaitzidou et al., 2019; Manceau and Charlet, 1994; Missana et al., 2009).

According to the EXAFS result, other types of sorption or retention mechanisms can be largely excluded. For instance, Missana et al. (2009) reported formation of a discrete ferric selenite phase like $Fe_2(SeO_3)_3 \cdot 6H_2O$ at pH 4. This would result in higher Fe coordination numbers as well as in the presence of additional Se backscatter atoms, which are both missing in our EXAFS data. However, the slightly increased iron coordination numbers of the pH 4 sample could indicate an incipient surface precipitation of ferric selenite in addition to inner-sphere selenite adsorption under acidic conditions, which has also been reported for selenite adsorption on ferrihydrite at low pH (Francisco et al., 2018). Also the formation of monodentate mononuclear corner-sharing [1]V complexes, which can arise for instance during the adsorption of As-oxyanions (arsenate or arsenite) on magnetite or maghemite can be ruled out (Morin et al., 2008; Navarathna et al., 2019; Zhang et al., 2011), since structural features in the EXAFS FT range beyond 3.5 Å are absent. Furthermore, we could exclude the presence of tridentate hexanuclear corner-sharing [3]C complexes, that have been shown to form with the oxyanions arsenite (Liu et al., 2015; Wang et al.,

2008) and antimonite (Kirsch et al., 2008) at the {111} faces of magnetite, since backscatterer atoms at higher atomic distances are absent. This assumption is supported by results of previous studies, in which also no hints for selenite [1]V or [3]C adsorption complexes on magnetite or maghemite have been found (Jordan et al., 2014; Missana et al., 2009). Jordan et al. (2014) explain this different behaviour of selenite compared to arsenite or antimonite by the different sizes of these trigonal pyramidal oxyanion molecules.

3.5. Properties and stability of the selenite surface complexes

Based on XAFS data, interaction of dissolved selenite with magnetite under oxic conditions leads to the simultaneous formation of [2]E and [2]C adsorption complexes. Which types of adsorption complexes develop on a particular material generally depends on the prevailing hydrochemical conditions and the structural and morphological properties of the adsorbent phase. This can be explained by the atomic structure and features of specific crystal surfaces. Due to the distinct arrangement of functional surface groups or, respectively, adsorption sites, certain types of adsorption complexes occur mainly on certain crystal surfaces. Since the affinity of an adsorbate for certain adsorption sites is determined among other things by its general surface coverage (Fukushi and Sverjensky, 2007; Peak and Sparks, 2002), which in turn is influenced by the pH value, different crystal surfaces show different reactivities depending on the degree of coverage or pH. Additionally, it must be considered that depending on the morphology of the nanoparticles, the exposed crystal faces may also vary. For oxyanion adsorption on
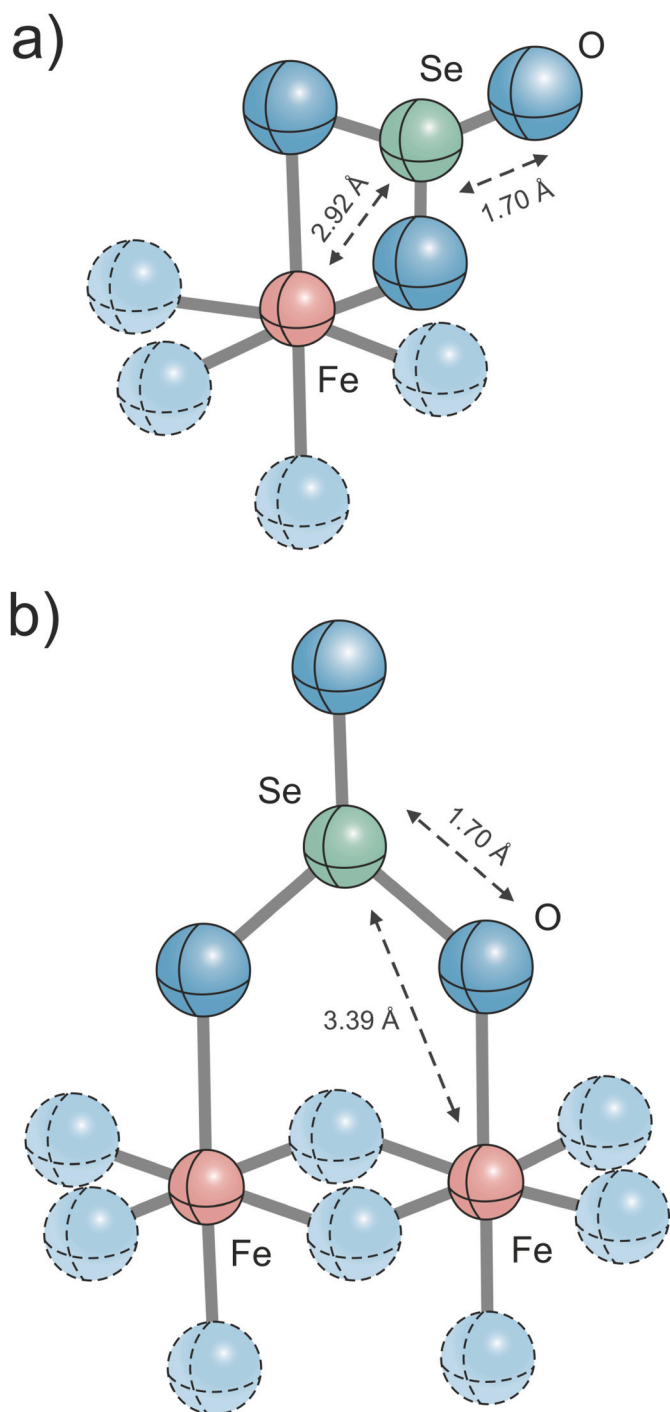
Fig. 5. Model showing the structure of (a) ^{2}E and (b) ^{2}C adsorption complexes between selenite molecules and FeO$_6$ octahedra.

magnetite and maghemite, formation of ^{2}C adsorption complexes is mainly associated with the {100} crystal surface, while the ^{2}E complexes are related to the {110} or {111} facets (Jonsson and Sherman, 2008; Jordan et al., 2014; Liu et al., 2015; Navarathna et al., 2019; Wang et al, 2008, 2011).

Changing selenite adsorption types depending on solution pH were determined by EXAFS analysis for both magnetite (Missana et al., 2009) and maghemite (Jordan et al., 2014). The respective results indicate that ^{2}E and ^{2}C selenite adsorption complexes appear simultaneously at acidic conditions or at high surface coverages, respectively, with the corner-sharing ^{2}C complexes being dominant. With increasing pH values

or decreasing surface coverages, the share of ^{2}C complexes tends to decrease and at alkaline conditions (>pH 8) only edge-sharing ^{2}E adsorption complexes occur. However, the authors of both studies noted that the evaluation of EXAFS data for such samples is quite difficult. Due to the small coordination numbers, especially at neutral or alkaline conditions, identification of the adsorption complexes as well as determination of their relative shares becomes more and more challenging. This challenge also arises for the EXAFS data of this work. Particularly the samples at pH 7 and pH 9.2 are characterized by small Fe coordination numbers, which makes it difficult to estimate their relative fractions.

We therefore performed a statistical analysis of the EXAFS spectra with Iterative Transformation Factor Analysis (ITFA) (Rossberg et al., 2003). ITFA allows determining the number of principal components (PC) and their respective factor loadings (Rossberg et al., 2009; Yalçintaş et al., 2016). Fig. 4a and b illustrates the good match between the experimental spectra (black) and their reconstructions (red lines) by two PC. The ITFA thus confirms that two individual spectral components are needed to characterize the EXAFS spectra of all three adsorption samples.

Moreover, the corresponding Varimax factor loadings (Fig. 4c) show that the sample at pH 4 is solely dominated by PC 1, whereas PC 2 primarily represents selenite adsorption under alkaline conditions. Based on the previous observations and the findings of Missana et al. (2009) and Jordan et al. (2014), these results can be interpreted in a way that the different factor loadings are associated with a varying distribution of ^{2}E and ^{2}C surface adsorption complexes. Accordingly, PC 1 reflects a combination of ^{2}E and ^{2}C adsorption complexes with a higher proportion of corner-sharing ^{2}C complexes, while PC 2 represents a mixture of both complexation types with a higher share of ^{2}E complexes. Under neutral or slightly alkaline conditions, both adsorption types would thus occur in approximately equal proportions, which is consistent with the factor loading of sample Se(IV)AdsMt-pH7.

The dependency of the complexation type from the pH value can basically be interpreted that increasing pH values and a higher negative surface charge cause a change in stability and thus in the predominance of certain selenite adsorption complexes. Under favourable adsorption conditions, the affinity of selenite oxyanions to form corner-sharing ^{2}C complexes is generally higher than for edge-sharing ^{2}E complexes, leading to a quantitative predominance of the ^{2}C complexes over a wide pH range. However, at more alkaline conditions, which are generally unfavourable for selenite adsorption, the ^{2}E complexes become more stable. This effect, which could be explained by the higher selectivity of ^{2}E sites for selenite, leads to a significant increase in the proportion of ^{2}E over ^{2}C complexes, although the absolute amount of adsorbed selenite decreases with increasing pH.

3.6. Environmental and technical application

Evidence of significant adsorption-based Se retention despite the lack of reduction contributes to understanding the retention behaviour of Se oxyanions in contact with nanoparticulate magnetite/maghemite phases in (sub)oxic environments. This scenario can be applied to various systems affected by Se contaminated groundwater and wastewater. Since magnetite occurs naturally in soil and sediments or can be derived via microbial pathways (Usman et al., 2018), adsorption of Se and other oxyanions on partially oxidized magnetite can be relevant for assessing contaminant fate in natural systems. This natural attenuation particularly concerns polluted oxic aquifers (e.g. Red River Delta, Vietnam; Kontny et al., 2021). Nevertheless, in natural environments, also the adverse influence of microbial processes must be considered, which can significantly reduce long-term retention of adsorbed Se oxyanions due to the formation of mobile and even volatile organic species (Peitzsch et al., 2010).

Other potential applications include *in situ* remediation techniques such as Se removal from wastewater using permeable reactive barrier

(PRB) technologies. In engineered PRB systems, a reactive medium is introduced into the subsurface to passively remove contaminants without additional treatment. Magnetite nanoparticles are not only a promising source material, but also a main corrosion product of (nanoscale) zero-valent iron (ZVI), which is often used for treating both inorganic and organic pollutants (Karn et al., 2009; Morrison et al., 2002; Roh et al., 2000). The adsorption-based retention described above could thus be of interest for settings where Se immobilization by reductive precipitation is not possible or inhibited (oxic conditions) or where the originally applied reactive material (e.g. ZVI) has lost its reducing ability. However, with respect to the stability of retention, the difference between Se reduction and precipitation of insoluble Se phases and formation of surface complexes has to be considered. This concerns in particular the unclear long-term stability of Se oxyanion surface complexes due to possible desorption caused by high pH, presence of competing anions or DOC, or reductive dissolution of the magnetite (Henderson and Demond, 2007; Su et al., 2007). In addition, colloidal transport of Se-loaded magnetite nanoparticles in flowing groundwater could affect Se mobility and prevent Se from remaining at the remediation site.

Affordable and easy-to-produce nanoparticles are also widely researched and used for *ex situ* or technical wastewater treatment applications. Among these, magnetite has emerged as suitable material due to its high reactivity combined with its magnetic properties (Carlos et al., 2013; Giraldo et al., 2013; Lankathilaka et al., 2021). The latter allows controlled use and easy separation after application (Yavuz et al., 2006). Based on our results, the addition of synthesized magnetite nanoparticles for remediation of contaminated wastewaters should also work with partially oxidized magnetite particles after oxidation or under oxic operating conditions, and not only under anoxic conditions causing Se reduction. Depending on the particular scenario, the total retention capacity would then even be defined by both redox transformation and adsorption processes. As for other materials, however, this approach would raise the question of whether exhausted magnetite can be regenerated and reactivated, e.g. through controlled desorption, or how the resulting contaminated magnetite sludges can be properly disposed of after their application.

A further relevant aspect of the demonstrated Se retention by adsorption is that surface complexation modeling can be applied to predict Se migration and optimize wastewater treatment in case of environments where reduction processes do not occur.

4. Conclusion

When redox-sensitive materials are considered to prevent the migration of pollutants, it must be taken into account that the retention properties of these materials can change considerably in natural environments. This study demonstrates that magnetite nanoparticles can effectively remediate selenite and selenate contaminated wastewaters even if they are partially oxidized. However, the retention requires suitable hydrochemical conditions, which mainly concern the prevailing pH and the corresponding selenium speciation. While retention of selenate only takes place at acidic conditions, selenite is immobilized over a large pH range. No reduction processes were involved in the immobilization. The specific retention mechanism is attributable to the formation of surface adsorption complexes. A mixture of mononuclear edge-sharing (^{2}E) and binuclear corner-sharing (^{2}C) inner-sphere complexes in case of selenite and most likely outer-sphere surface complexes in case of selenate. It was found that both types of inner-sphere selenite complexes have different affinities and stabilities depending on the solution pH.

Regarding the assessment of the remediation efficiency of oxidized magnetite, the results show that the mechanisms of selenate and selenate adsorption are comparable to the findings from previous adsorption studies on pure maghemite. Accordingly, in systems where no reduction takes place, partially oxidized magnetite nanoparticles can

approximately be considered as a maghemite-like adsorbent phase. These findings help to better understand the retention behaviour of selenium oxyanions in contact with nanoparticulate magnetite/maghemite phases under (sub)oxic conditions and could be used in modeling the migration of selenium oxyanions in natural and engineered systems.

Declaration of competing interest

The authors declare that they have no known competing financial interests or personal relationships that could have appeared to influence the work reported in this paper.

There are no conflicts of interest to declare.

Appendix A. Supplementary data

Supplementary data to this article can be found online at https://doi.org/10.1016/j.apgeochem.2021.105062.

References

Ankudinov, A.L., Rehr, J.J., 1997. Relativistic calculations of spin-dependent x-ray-absorption spectra. Phys. Rev. B 56, 1712–1715. https://doi.org/10.1103/PhysRevB.56.R1712.

Bingham, P.A., Connelly, A.J., Cassingham, N.J., Hyatt, N.C., 2011. Oxidation state and local environment of selenium in alkali borosilicate glasses for radioactive waste immobilisation. J. Non-Cryst. Solids 357, 2726–2734. https://doi.org/10.1016/j.jnoncrysol.2010.12.053.

Borsig, N., Scheinost, A.C., Shaw, S., Schild, D., Neumann, T., 2018. Retention and multiphase transformation of selenium oxyanions during the formation of magnetite via iron(II) hydroxide and green rust. Dalton Trans. 47, 11002–11015. https://doi.org/10.1039/c8dt01799a.

Borsig, N., Scheinost, A.C., Shaw, S., Schild, D., Neumann, T., 2017. Uptake mechanisms of selenium oxyanions during the ferrihydrite-hematite recrystallization. Geochem. Cosmochim. Acta 206, 236–253. https://doi.org/10.1016/j.gca.2017.03.004.

Carlos, L., García Einschlag, F.S., González, M.C., Mártire, D.O., 2013. Applications of magnetite nanoparticles for heavy metal removal from wastewater. In: Waste Water - Treatment Technologies and Recent Analytical Developments. InTech. https://doi.org/10.5772/54608.

Chan, Y.T., Kuan, W.H., Chen, T.Y., Wang, M.K., 2009. Adsorption mechanism of selenate and selenite on the binary oxide systems. Water Res. 43, 4412–4420. https://doi.org/10.1016/j.watres.2009.06.056.

Charlet, L., Scheinost, A.C., Tournassat, C., Greneche, J.M., Géhin, A., Fernández-Martínez, A., Coudert, S., Tisserand, D., Brendle, J., 2007. Electron transfer at the mineral/water interface: selenium reduction by ferrous iron sorbed on clay. Geochem. Cosmochim. Acta 71, 5731–5749. https://doi.org/10.1016/j.gca.2007.08.024.

Chowdhury, S.R., Yanful, E.K., 2010. Arsenic and chromium removal by mixed magnetite-maghemite nanoparticles and the effect of phosphate on removal. J. Environ. Manag. 91, 2238–2247. https://doi.org/10.1016/j.jenvman.2010.06.003.

Cornell, R.M., Schwertmann, U., 2003. The Iron Oxides: Structure, Properties, Reactions. Occurences and Uses, second ed. Wiley-VCH, Weinheim, Germany. https://doi.org/10.1002/3527602097.

De Cannière, P., Maes, A., Williams, S., Bruggeman, C., Beauwens, T., Maes, N., Cowper, M., 2010. Behaviour of Selenium in Boom Clay. External Report of the Belgian Nuclear Research Centre. SCK•CEN-ER-120, Mol, BEL.

Dhillon, K.S., Dhillon, S.K., 2003. Distribution and management of seleniferous soils. Adv. Agron. 79, 119–184. https://doi.org/10.1016/S0065-2113(02)79003-2.

Duc, M., Lefèvre, G., Fédoroff, M., Jeanjean, J., Rouchaud, J.C., Monteil-Rivera, F., Dumonceau, J., Milonjic, S., 2003. Sorption of selenium anionic species on apatites and iron oxides from aqueous solutions. J. Environ. Radioact. 70, 61–72. https://doi.org/10.1016/S0265-931X(03)00125-5.

Fernández-Martínez, A., Charlet, L., 2009. Selenium environmental cycling and bioavailability: a structural chemist point of view. Rev. Environ. Sci. Biotechnol. 8, 81–110. https://doi.org/10.1007/s11157-009-9145-3.

Francisco, P.C.M., Sato, T., Otake, T., Kasama, T., Suzuki, S., Shiwaku, H., Yaita, T., 2018. Mechanisms of Se(IV) Co-precipitation with ferrihydrite at acidic and alkaline conditions and its behavior during aging. Environ. Sci. Technol. 52, 4817–4826. https://doi.org/10.1021/acs.est.8b00462.

Frechou, C., Aguerre, S., Degros, J.P., Kerlau, G., Grangeon, T., 2007. Improvement of a radiochemical separation for selenium 79: applications to effluents and nuclear wastes. Talanta 72, 1166–1171. https://doi.org/10.1016/j.talanta.2007.01.011.

Fukushi, K., Sverjensky, D.A., 2007. A surface complexation model for sulfate and selenate on iron oxides consistent with spectroscopic and theoretical molecular evidence. Geochem. Cosmochim. Acta 71, 1–24. https://doi.org/10.1016/j.gca.2006.08.048.

Génin, J.-M.R., Ruby, C., Géhin, A., Refait, P., 2006. Synthesis of green rusts by oxidation of Fe(OH)₂, their products of oxidation and reduction of ferric oxyhydroxides; Eh-pH Pourbaix diagrams. Compt. Rendus Geosci. 338, 433–446. https://doi.org/10.1016/j.crte.2006.04.004.

Giraldo, L., Erto, A., Moreno-Piraján, J.C., 2013. Magnetite nanoparticles for removal of heavy metals from aqueous solutions: synthesis and characterization. Adsorption 19, 465–474. https://doi.org/10.1007/s10450-012-9468-1.

Gonzalez, C.M., Hernandez, J., Parsons, J.G., Gardea-Torresdey, J.L., 2010. A study of the removal of selenite and selenate from aqueous solutions using a magnetic iron/manganese oxide nanomaterial and ICP-MS. Microchem. J. 96, 324–329. https://doi.org/10.1016/j.microc.2010.05.005.

Gorski, C.A., Scherer, M.M., 2010. Determination of nanoparticulate magnetite stoichiometry by Mossbauer spectroscopy, acidic dissolution, and powder X-ray diffraction: a critical review. Am. Mineral. 95, 1017–1026. https://doi.org/10.2138/am.2010.3435.

Hawthorne, F.C., 1984. The crystal structure of mandarinoite, Fe³⁺₂Se₃O₉·6H₂O. Can. Mineral. 22, 475–480.

Hayes, K.F., Roe, A.L., Brown, G.E., Hodgson, K.O., Leckie, J.O., Parks, G.A., 1987. In situ X-ray absorption study of surface complexes: selenium oxyanions on α-FeOOH. Science 238, 783–786. https://doi.org/10.1126/science.238.4828.783.

He, Y.T., Traina, S.J., 2005. Cr(VI) reduction and immobilization by magnetite under alkaline pH conditions: the role of passivation. Environ. Sci. Technol. 39, 4499–4504. https://doi.org/10.1021/es0483692.

Henderson, A.D., Demond, A.H., 2007. Long-term performance of zero-valent iron permeable reactive barriers: a critical review. Environ. Eng. Sci. 24, 401–423. https://doi.org/10.1089/ees.2006.0071.

Hiemstra, T., Rietra, R.P.JJ., Van Riemsdijk, W.H., 2007. Surface complexation of selenite on goethite: MO/DFT geometry and charge distribution. Croat. Chem. Acta 80, 313–324.

Horst, M.F., Lassalle, V., Ferreira, M.L., 2015. Nanosized magnetite in low cost materials for remediation of water polluted with toxic metals, azo- and antraquinonic dyes. Front. Environ. Sci. Eng. 9, 746–769. https://doi.org/10.1007/s11783-015-0814-x.

Hu, J.D., Zevi, Y., Kou, X.M., Xiao, J., Wang, X.J., Jin, Y., 2010. Effect of dissolved organic matter on the stability of magnetite nanoparticles under different pH and ionic strength conditions. Sci. Total Environ. 408, 3477–3489. https://doi.org/10.1016/j.scitotenv.2010.03.033.

Huber, F., Schild, D., Vitova, T., Rothe, J., Kirsch, R., Schafer, T., 2012. U(VI) removal kinetics in presence of synthetic magnetite nanoparticles. Geochem. Cosmochim. Acta 96, 154–173. https://doi.org/10.1016/j.gca.2012.07.019.

Iwatsuki, M., Fukasawa, T., 1993. Nondestructive and complete analysis of magnetite-maghemite solid solutions by a combined X-ray diffraction/fluorescence method. Anal. Sci. 9, 95–98. https://doi.org/10.2116/analsci.9.95.

Iyengar, S.J., Joy, M., Ghosh, C.K., Dey, S., Kotnala, R.K., Ghosh, S., 2014. Magnetic, X-ray and Mossbauer studies on magnetite/maghemite core-shell nanostructures fabricated through an aqueous route. RSC Adv. 4, 64919–64929. https://doi.org/10.1039/c4ra11283k.

Jonsson, J., Sherman, D.M., 2008. Sorption of As(III) and As(V) to siderite, green rust (fougerite) and magnetite: implications for arsenic release in anoxic groundwaters. Chem. Geol. 255, 173–181. https://doi.org/10.1016/j.chemgeo.2008.06.036.

Jordan, N., Lomenech, C., Marmier, N., Giffaut, E., Ehrhardt, J.J., 2009. Sorption of selenium(IV) onto magnetite in the presence of silicic acid. J. Colloid Interface Sci. 329, 17–23. https://doi.org/10.1016/j.jcis.2008.09.052.

Jordan, N., Ritter, A., Foerstendorf, H., Scheinost, A.C., Weiß, S., Heim, K., Grenzer, J., Mücklich, A., Reuther, H., 2013. Adsorption mechanism of selenium(VI) onto maghemite. Geochem. Cosmochim. Acta 103, 63–75. https://doi.org/10.1016/j.gca.2012.09.048.

Jordan, N., Ritter, A., Scheinost, A.C., Weiss, S., Schild, D., Hübner, R., 2014. Selenium (IV) uptake by maghemite (γ-Fe₂O₃). Environ. Sci. Technol. 48, 1665–1674. https://doi.org/10.1021/es4045852.

Kalaitzidou, K., Nikoletopoulos, A.-A., Tsiftsakis, N., Pinakidou, F., Mitrakas, M., 2019. Adsorption of Se(IV) and Se(VI) species by iron oxy-hydroxides: effect of positive surface charge density. Sci. Total Environ. 687, 1197–1206. https://doi.org/10.1016/j.scitotenv.2019.06.174.

Karn, B., Kuiken, T., Otto, M., 2009. Nanotechnology and in situ remediation: a review of the benefits and potential risks. Environ. Health Perspect. 117, 1823–1831. https://doi.org/10.1289/ehp.0900793.

Khan, U.S., Amanullah, Manan, A., Khan, N., Mahmood, A., Rahim, A., 2015. Transformation mechanism of magnetite nanoparticles. Mater. Sci. Pol 33, 278–285. https://doi.org/10.1515/msp-2015-0037.

Kim, S.S., Min, J.H., Lee, J.K., Baik, M.H., Choi, J.-W., Shin, H.S., 2012. Effects of pH and anions on the sorption of selenium ions onto magnetite. J. Environ. Radioact. 104, 1–6. https://doi.org/10.1016/j.jenvrad.2011.09.013.

Kim, W., Suh, C.Y., Cho, S.W., Roh, K.M., Kwon, H., Song, K., Shon, I.J., 2012. A new method for the identification and quantification of magnetite-maghemite mixture using conventional X-ray diffraction technique. Talanta 94, 348–352. https://doi.org/10.1016/j.talanta.2012.03.001.

Kirsch, R., Scheinost, A.C., Rossberg, A., Banerjee, D., Charlet, L., 2008. Reduction of antimony by nano-particulate magnetite and mackinawite. Mineral. Mag. 72, 185–189. https://doi.org/10.1180/minmag.2008.072.1.185.

Kontny, A., Schneider, M., Eiche, E., Stopelli, E., Glodowska, M., Rathi, B., Gottlicher, J., Byrne, J.M., Kappler, A., Berg, M., Thi, D.V., Trang, P.T.K., Viet, P.H., Neumann, T., 2021. Iron mineral transformations and their impact on as (im)mobilization at redox interfaces in As-contaminated aquifers. Geochem. Cosmochim. Acta 296, 189–209. https://doi.org/10.1016/j.gca.2020.12.029.

Kosmulski, M., 2020. The pH dependent surface charging and points of zero charge. VIII. Update. Adv. Colloid Interface Sci. 275, 102064 https://doi.org/10.1016/j.cis.2019.102064.

Kuhn, L.T., Bojesen, A., Timmermann, L., Nielsen, M.M., Mørup, S., 2002. Structural and magnetic properties of core-shell iron-iron oxide nanoparticles. J. Phys. Condens. Matter 14, 13551–13567. https://doi.org/10.1088/0953-8984/14/49/311.

Kuppusamy, S., Palanisami, T., Megharaj, M., Venkateswarlu, K., Naidu, R., 2016. In-situ remediation approaches for the management of contaminated sites: a comprehensive overview. Rev. Environ. Contam. Toxicol. 236, 1–115. https://doi.org/10.1007/978-3-319-20013-2_1.

Lankathilaka, K.P.W., de Silva, R.M., Mantilaka, M.M.M.G.P.G., de Silva, K.M.N., 2021. Magnetite nanoparticles incorporated porous kaolin as a superior heavy metal sorbent for water purification. Groundw. Sustain. Dev. 14, 100606 https://doi.org/10.1016/j.gsd.2021.100606.

Latta, D.E., Gorski, C.A., Boyanov, M.I., O'Loughlin, E.J., Kemner, K.M., Scherer, M.M., 2012. Influence of magnetite stoichiometry on U^VI reduction. Environ. Sci. Technol. 46, 778–786. https://doi.org/10.1021/es2024912.

Lemly, A.D., 2004. Aquatic selenium pollution is a global environmental safety issue. Ecotoxicol. Environ. Saf. 59, 44–56. https://doi.org/10.1016/S0147-6513(03)00095-2.

Lenz, M., Lens, P.N.L., 2009. The essential toxin: the changing perception of selenium in environmental sciences. Sci. Total Environ. 407, 3620–3633. https://doi.org/10.1016/j.scitotenv.2008.07.056.

Li, Z., Chanéac, C., Berger, G., Delaunay, S., Graff, A., Lefèvre, G., 2019. Mechanism and kinetics of magnetite oxidation under hydrothermal conditions. RSC Adv. 9, 33633–33642. https://doi.org/10.1039/c9ra03234g.

Li, Z., Liu, M., Chen, L.K., Li, G.Z., 2017. Combined toxicity of an environmental remediation residue, magnetite Fe₃O₄ nanoparticles/Cr(VI) adduct. Biomed. Environ. Sci. 30, 783–791. https://doi.org/10.3967/bes2017.106.

Liu, A., Liu, J., Pan, B., Zhang, W.X., 2014. Formation of lepidocrocite (γ-FeOOH) from oxidation of nanoscale zero-valent iron (nZVI) in oxygenated water. RSC Adv. 4, 57377–57382. https://doi.org/10.1039/c4ra08988j.

Liu, C.H., Chuang, Y.H., Chen, T.Y., Tian, Y., Li, H., Wang, M.K., Zhang, W., 2015. Mechanism of arsenic adsorption on magnetite nanoparticles from water: thermodynamic and spectroscopic studies. Environ. Sci. Technol. 49, 7726–7734. https://doi.org/10.1021/acs.est.5b00381.

Loyo, R.L., de, A., Nikitenko, S.I., Scheinost, A.C., Simonoff, M., 2008. Immobilization of selenite on Fe₃O₄ and Fe/Fe₃C ultrasmall particles. Environ. Sci. Technol. 42, 2451–2456.

Manceau, A., Charlet, L., 1994. The mechanism of selenate adsorption on goethite and hydrous ferric oxide. J. Colloid Interface Sci. 168, 87–93. https://doi.org/10.1006/jcis.1994.1396.

Martínez, M., Giménez, J., de Pablo, J., Rovira, M., Duro, L., 2006. Sorption of selenium (IV) and selenium(VI) onto magnetite. Appl. Surf. Sci. 252, 3767–3773. https://doi.org/10.1016/j.apsusc.2005.05.067.

Matulová, M., Urík, M., Bujdoš, M., Duborská, E., Cesnek, M., Miglierini, M.B., 2019. Selenite sorption onto goethite: isotherm and ion-competitive studies, and effect of pH on sorption kinetics. Chem. Pap. 73, 2975–2985. https://doi.org/10.1007/s11696-019-00847-1.

Milonjić, S.K., Kopečni, M.M., Ilić, Z.E., 1983. The point of zero charge and adsorption properties of natural magnetite. J. Radioanal. Chem. 78, 15–24. https://doi.org/10.1007/BF02519745.

Missana, T., Alonso, U., Scheinost, A.C., Granizo, N., García-Gutiérrez, M., 2009. Selenite retention by nanocrystalline magnetite: role of adsorption, reduction and dissolution/co-precipitation processes. Geochem. Cosmochim. Acta 73, 6205–6217. https://doi.org/10.1016/j.gca.2009.07.005.

Morin, G., Ona-Nguema, G., Wang, Y., Menguy, N., Juillot, F., Proux, O., Guyot, F., Calas, G., Brown, G.E., 2008. Extended X-ray absorption fine structure analysis of arsenite and arsenate adsorption on maghemite. Environ. Sci. Technol. 42, 2361–2366. https://doi.org/10.1021/es072057s.

Morrison, S.J., Metzler, D.R., Dwyer, B.P., 2002. Removal of As, Mn, Mo, Se, U, V and Zn from groundwater by zero-valent iron in a passive treatment cell: reaction progress modeling. J. Contam. Hydrol. 56, 99–116. https://doi.org/10.1016/S0169-7722(01)00205-4.

Mu, Y., Jia, F., Ai, Z., Zhang, L., 2017. Iron oxide shell mediated environmental remediation properties of nano zero-valent iron. Environ. Sci. Nano 4, 27–45. https://doi.org/10.1039/C6EN00398B.

Munier-Lamy, C., Deneux-Mustin, S., Mustin, C., Merlet, D., Berthelin, J., Leyval, C., 2007. Selenium bioavailability and uptake as affected by four different plants in a loamy clay soil with particular attention to mycorrhizae inoculated ryegrass. J. Environ. Radioact. 97, 148–158. https://doi.org/10.1016/j.jenvrad.2007.04.001.

Nakamaru, Y.M., Altansuvd, J., 2014. Speciation and bioavailability of selenium and antimony in non-flooded and wetland soils: a review. Chemosphere 111, 366–371. https://doi.org/10.1016/j.chemosphere.2014.04.024.

Navarathna, C.M., Karunanayake, A.G., Gunatilake, S.R., Pittman, C.U., Perez, F., Mohan, D., Mlsna, T., 2019. Removal of Arsenic(III) from water using magnetite precipitated onto Douglas fir biochar. J. Environ. Manag. 250, 109429 https://doi.org/10.1016/j.jenvman.2019.109429.

Peak, D., Sparks, D.L., 2002. Mechanisms of selenate adsorption on iron oxides and hydroxides. Environ. Sci. Technol. 36, 1460–1466. https://doi.org/10.1021/es0156643.

Peitzsch, M., Kremer, D., Kersten, M., 2010. Microfungal alkylation and volatilization of selenium adsorbed by goethite. Environ. Sci. Technol. 44, 129–135. https://doi.org/10.1021/es9006492.

Rebodos, R.L., Vikesland, P.J., 2010. Effects of oxidation on the magnetization of nanoparticulate magnetite. Langmuir 26, 16745–16753. https://doi.org/10.1021/la102461z.

Ressler, T., 1998. WinXAS: a program for X-ray absorption spectroscopy data analysis under MS-Windows. J. Synchrotron Radiat. 5, 118–122. https://doi.org/10.1107/S0909049597019298.

Rietra, R.P.J.J., Hiemstra, T., van Riemsdijk, W.H., 2001. Comparison of selenate and sulfate adsorption on goethite. J. Colloid Interface Sci. 240, 384–390. https://doi.org/10.1006/jcis.2001.7650.

Roh, Y., Lee, S.Y., Elless, M.P., 2000. Characterization of corrosion products in the permeable reactive barriers. Environ. Geol. 40, 184–194. https://doi.org/10.1007/s002540000178.

Rossberg, A., Reich, T., Bernhard, G., 2003. Complexation of uranium(VI) with protocatechuic acid-application of iterative transformation factor analysis to EXAFS spectroscopy. Anal. Bioanal. Chem. 376, 631–638. https://doi.org/10.1007/s00216-003-1963-5.

Rossberg, A., Ulrich, K.U., Weiss, S., Tsushima, S., Hiemstra, T., Scheinost, A.C., 2009. Identification of uranyl surface complexes on ferrihydrite: advanced EXAFS data analysis and CD-music modeling. Environ. Sci. Technol. 43, 1400–1406. https://doi.org/10.1021/es801727w.

Rovira, M., Giménez, J., Martínez, M., Martínez-Lladó, X., de Pablo, J., Martí, V., Duro, L., 2008. Sorption of selenium(IV) and selenium(VI) onto natural iron oxides: goethite and hematite. J. Hazard Mater. 150, 279–284. https://doi.org/10.1016/j.jhazmat.2007.04.098.

Salah, S., Wang, L., 2014. Speciation and Solubility Calculations for Waste Relevant Radionuclides in Boom Clay. External Report of the Belgian Nuclear Research Centre. SCK•CEN-ER-198, Mol, BEL.

Salazar Camacho, C.A., Villalobos Penalosa, M., 2017. Characterization and surface reactivity of natural and synthetic magnetites: II. Adsorption of Pb(II) and Zn(II). Rev. Int. Contam. Ambient. 33, 165–176. https://doi.org/10.20937/RICA.2017.33.01.15.

Scheinost, A.C., Charlet, L., 2008. Selenite reduction by mackinawite, magnetite and siderite: XAS characterization of nanosized redox products. Environ. Sci. Technol. 42, 1984–1989. https://doi.org/10.1021/es071573f.

Scheinost, A.C., Kirsch, R., Banerjee, D., Fernandez-Martinez, A., Zaenker, H., Funke, H., Charlet, L., 2008. X-ray absorption and photoelectron spectroscopy investigation of selenite reduction by Fe^{II}-bearing minerals. J. Contam. Hydrol. 102, 228–245. https://doi.org/10.1016/j.jconhyd.2008.09.018.

Séby, F., Potin-Gautier, M., Giffaut, E., Borge, G., Donard, O.F.X., 2001. A critical review of thermodynamic data for selenium species at 25°C. Chem. Geol. 171, 173–194. https://doi.org/10.1016/S0009-2541(00)00246-1.

Sharifi Dehsari, H., Ksenofontov, V., Moller, A., Jakob, G., Asadi, K., 2018. Determining magnetite/maghemite composition and core-shell nanostructure from magnetization curve for iron oxide nanoparticles. J. Phys. Chem. C 122, 28292–28301. https://doi.org/10.1021/acs.jpcc.8b06927.

Signorini, L., Pasquini, L., Savini, L., Carboni, R., Boscherini, F., Bonetti, E., Giglia, A., Pedio, M., Mahne, N., Mahne, N., Nannarone, S., Nannarone, S., 2003. Size-dependent oxidation in iron/iron oxide core-shell nanoparticles. Phys. Rev. B Condens. Matter 68, 1–8. https://doi.org/10.1103/PhysRevB.68.195423.

Su, C., Ford, R.G., Wilkin, R.T., 2007. Selenium. In: Ford, R.G., Wilkin, R.T., Puls, R.W. (Eds.), Monitored Natural Attenuation of Inorganic Contaminants in Ground Water: Volume 2-Assessment for Non-radionuclides Including Arsenic, Cadmium, Chromium, Copper, Lead, Nickel, Nitrate, Perchlorate, and Selenium. US EPA, Oklahoma, USA, pp. 72–85.

Su, C., Suarez, D.L., 2000. Selenate and selenite sorption on iron oxides. Soil Sci. Soc. Am. J. 64, 101–111. https://doi.org/10.2136/sssaj2000.641101x.

Tan, L.C., Nancharaiah, Y.V., van Hullebusch, E.D., Lens, P.N.L., 2016. Selenium: environmental significance, pollution, and biological treatment technologies. Biotechnol. Adv. 34, 886–907. https://doi.org/10.1016/j.biotechadv.2016.05.005.

Usman, M., Byrne, J.M., Chaudhary, A., Orsetti, S., Hanna, K., Ruby, C., Kappler, A., Haderlein, S.B., 2018. Magnetite and green rust: synthesis, properties, and environmental applications of mixed-valent iron minerals. Chem. Rev. 118, 3251–3304. https://doi.org/10.1021/acs.chemrev.7b00224.

Verbinnen, B., Block, C., Lievens, P., Van Brecht, A., Vandecasteele, C., 2013. Simultaneous removal of molybdenum, antimony and selenium oxyanions from wastewater by adsorption on supported magnetite. Waste and Biomass Valorization 4, 635–645. https://doi.org/10.1007/s12649-013-9200-8.

Wang, Y., Morin, G., Ona-Nguema, G., Juillot, F., Calas, G., Brown, G.E., 2011. Distinctive arsenic(V) trapping modes by magnetite nanoparticles induced by different sorption processes. Environ. Sci. Technol. 45, 7258–7266. https://doi.org/10.1021/es200299f.

Wang, Y., Morin, G., Ona-Nguema, G., Menguy, N., Juillot, F., Aubry, E., Guyot, F., Calas, G., Brown, G.E., 2008. Arsenite sorption at the magnetite-water interface during aqueous precipitation of magnetite: EXAFS evidence for a new arsenite surface complex. Geochem. Cosmochim. Acta 72, 2573–2586. https://doi.org/10.1016/j.gca.2008.03.011.

Wei, X., Bhojappa, S., Lin, L.S., Viadero, R.C., 2012. Performance of nano-magnetite for removal of selenium from aqueous solutions. Environ. Eng. Sci. 29, 526–532. https://doi.org/10.1089/ees.2011.0383.

Weidner, E., Ciesielczyk, F., 2019. Removal of hazardous oxyanions from the environment using metal-oxide-based materials. Materials 12, 927. https://doi.org/10.3390/ma12060927.

Wilkin, R.T., Su, C., Ford, R.G., Paul, C.J., 2005. Chromium-removal processes during groundwater remediation by a zerovalent iron permeable reactive barrier. Environ. Sci. Technol. 39, 4599–4605. https://doi.org/10.1021/es050157x.

Wylie, E.M., Olive, D.T., Powell, B.A., 2016. Effects of titanium doping in titanomagnetite on neptunium sorption and speciation. Environ. Sci. Technol. 50, 1853–1858. https://doi.org/10.1021/acs.est.5b05339.

Yalçintaş, E., Scheinost, A.C., Gaona, X., Altmaier, M., 2016. Systematic XAS study on the reduction and uptake of Tc by magnetite and mackinawite. Dalton Trans. 45, 17874–17885. https://doi.org/10.1039/c6dt02872a.

Yavuz, C.T., Mayo, J.T., Yu, W.W., Prakash, A., Falkner, J.C., Yean, S., Cong, L., Shipley, H.J., Kan, A., Tomson, M., Natelson, D., Colvin, V.L., 2006. Low-field magnetic separation of monodisperse Fe$_3$O$_4$ nanocrystals. Science 314, 964–967. https://doi.org/10.1126/science.1131475.

Zhang, M., Pan, G., Zhao, D., He, G., 2011. XAFS study of starch-stabilized magnetite nanoparticles and surface speciation of arsenate. Environ. Pollut. 159, 3509–3514. https://doi.org/10.1016/j.envpol.2011.08.017.

Mechanisms of selenium removal by partially oxidized magnetite nanoparticles for wastewater remediation

Nicolas Börsig [a,*], Andreas C. Scheinost [b,c], Dieter Schild [d], Thomas Neumann [e]

[a] Karlsruhe Institute of Technology (KIT), Institute of Applied Geosciences, Adenauerring 20b, 76131 Karlsruhe, Germany

[b] Helmholtz-Zentrum Dresden-Rossendorf (HZDR), Institute of Resource Ecology, Bautzner Landstraße 400, 01328 Dresden, Germany

[c] The Rossendorf Beamline (ROBL) at ESRF, 38043 Grenoble, France

[d] Karlsruhe Institute of Technology (KIT), Institute for Nuclear Waste Disposal, Hermann-von-Helmholtz-Platz 1, 76344 Eggenstein-Leopoldshafen, Germany

[e] Technische Universität Berlin, Institute of Applied Geosciences, Ernst-Reuter-Platz 1, 10587 Berlin, Germany

* Corresponding author: Tel.: +49 721 608-44878; nicolas.boersig@kit.edu (N. Börsig)

Content:

Number of figures: 7

Number of tables: 3

Number of pages: 11

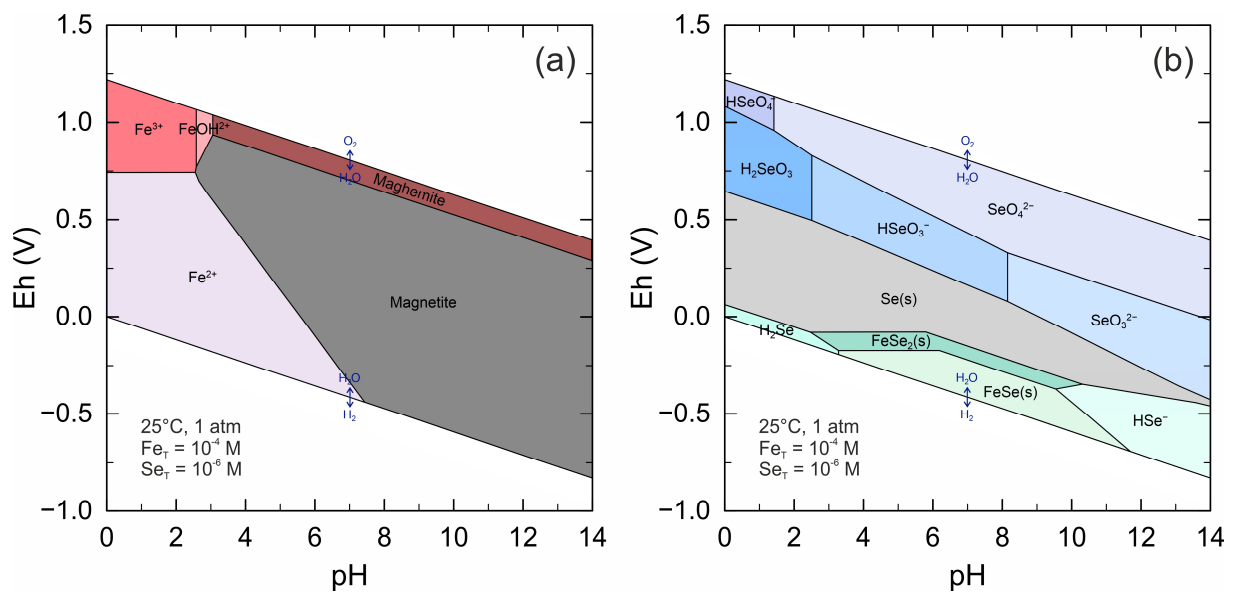# 1 Redox sensitivity of iron and selenium in aqueous solutions

Figure S1. Pourbaix diagrams of the Fe-Se-H₂O system at 25°C and 1 atm; Fe$_T$: 10^{-4} mol/L; Se$_T$: 10^{-6} mol/L. (a) Eh-pH diagram for iron considering the iron oxide minerals magnetite [Fe₃O₄] and maghemite [γ-Fe₂O₃]. (b) Eh-pH diagram for selenium taking into account different solid Fe and Se phases. Diagrams calculated with PHREEQC (USGS) using an adapted *wateq4f* database; thermodynamic Se data: aquatic species from Séby et al. (2001), solid phases from Salah and Wang (2014).

2 Detailed information about synthesis and analytical techniques
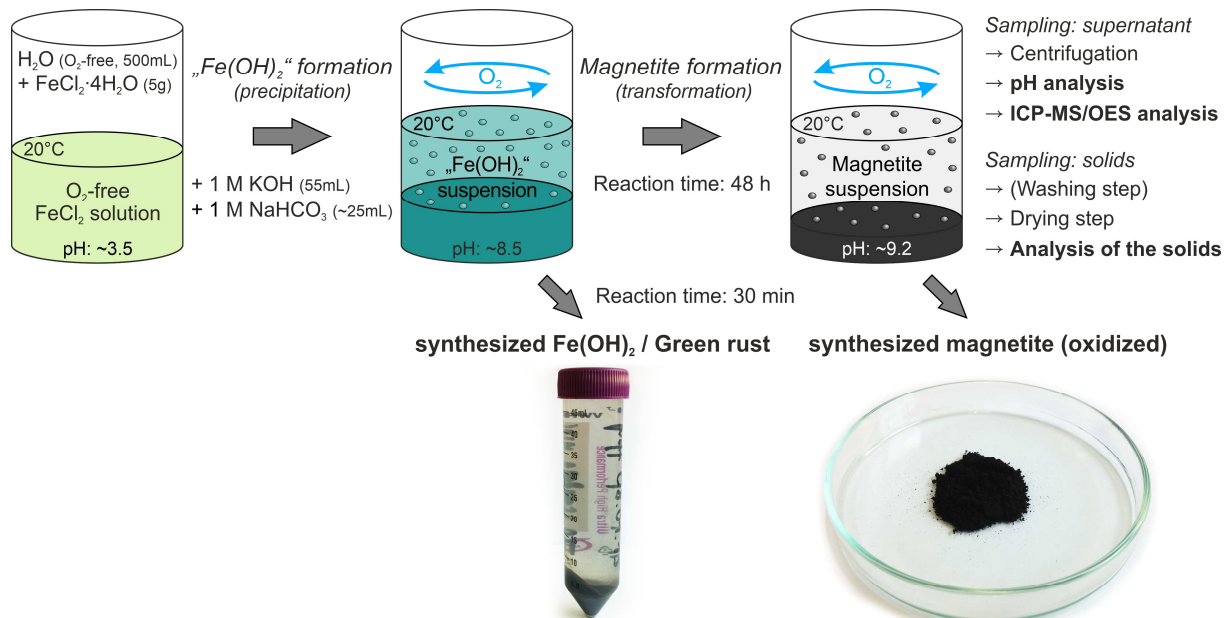
2.1 Magnetite synthesis

Figure S2. Schematic illustration of the magnetite synthesis process based on the by progressive oxidation of an aquatic Fe²⁺ solution and the subsequent sample treatment.

2

Table S1: Protocol of the pH history during the magnetite synthesis; all solutions used were prepared with N_2-degassed Milli-Q water.

Synthesis step		pH	Temp [°C]	O_2 (%)	O_2 (mg/L)
	5 g $FeCl_2 \cdot 4\,H_2O$ (5 g) + 500 mL H_2O	3.4	24.7	-	-
Addition:	+ 55 mL 1 M KOH	8.2	25.1	-	-
Addition:	+ 25 mL 1 M $NaHCO_3$	8.6	25.1	1.4	0.17
Time:	after 48 hours	9.2	24.9	87.8	7.15

Reaction product: Black precipitate

2.2 ICP-OES and ICP-MS

After centrifugation and filtration (0.2 µm filter), all supernatants were acidified with concentrated high-purity HNO_3 (50 µL). The Se and Fe concentrations in the aqueous phase were determined by ICP-OES (Inductively Coupled Plasma Optical Emission Spectrometry) or ICP-MS (Inductively Coupled Plasma Mass Spectrometry) depending on the Se concentrations: For amounts higher than 1 mg/L, measurements were performed on ICP-OES using a Varian 715ES. Analysis of samples with lower Se concentrations were carried out on an X-Series 2 ICP-MS (Thermo Fisher Scientific Inc.).

In case of ICP-MS analysis collision cell mode was used to eliminate polyatomic clusters, and Se and Fe isotopes (m/z: 76, 77, 78 for Se; 56 for Fe) without spectroscopic interferences were selected for detection. ^{45}Sc, ^{103}Rh, and ^{115}In were used as internal standards to minimize non-spectroscopic interferences. This includes the correction of signal changes caused by high ionic strength in some of the sample matrices.

The ICP-MS detection limits were approx. 0.3 µg/L for both Se and Fe, while the ICP-OES detection limit for Fe was approx. 12 µg/L. Throughout the analyses of both ICP methods, a certified reference solution was used as standard.

2.3 XRD

X-Ray Diffraction (XRD) was used for analysis of the purity and composition of the synthesized solid materials and performed on a Bruker D8 Advance X-ray diffractometer with Cu Kα radiation (λ = 1.5406 Å) and a LynxEye detector. Magnetite samples (reaction time: 48 h) were prepared from powders. XRD patterns of the analysed samples were compared with mineral references of the ICDD PDF-2 database.

2.4 BET

BET measurements were conducted on pure magnetite as well as on its precursor phase using a Quantachrome Autosorb 1-MP and 11-point BET-argon isotherms recorded at the temperature of liquid argon (87.3K) to calculate the specific surface areas (SSA). Prior to the measurement,

the sample were outgassed in vacuum at 95℃ overnight to remove water and other volatile surface contaminations. Note that the sample drying might has changed the characteristics of the solid phase in case of the redox-sensitive magnetite precursor phase.

2.5 pEDXRF

The Se content of the solid phases was determined by polarized Energy Dispersive X-ray Fluorescence Spectroscopy (pEDXRF) using an Epsilon 5 (PANalytical) equipped with a W X-ray tube and a Ge detector. A Mo target was selected as polarizing secondary target and the measurement period was 500 s, resulting in a lower detection limit for Se of 10 ppm and an analytical precision of ± 5%. Prepared standards consisting of mixtures of synthesized pure hematite and known amounts of a Se reference material (pure Se(0) powder or certified Se reference solution) were utilized for calibration.

2.6 SEM & EDX

SEM images were obtained using a LEO 1530 (Zeiss Inc.) scanning electron microscope (operated at 10 kV) with a NORAN System SIX (Thermo Electron Corp.) EDX-System. The dried powder samples (reaction time: 48 h) were coated with Pt after they were mounted on sample holders via double-sided carbon tape. Increased levels of C and Pt in EDX spectra are due to the characteristics of the sample holders and the Pt coating of the samples.

2.7 XPS

XPS measurements were performed using a PHI 5000 VersaProbe II (ULVAC-PHI Inc.). The system was equipped with a scanning microprobe X-ray source (monochromatic Al Kα, 1486.7 eV) in combination with an electron flood gun and a floating ion gun generating low-energy electrons (1 eV) and low energy argon ions (6 eV) for charge compensation at isolating samples (dual beam technique), respectively. Calibration of the binding energy scale of the spectrometer was performed using the well-established binding energies of elemental lines of pure metals (monochromatic Al Kα: Cu $2p_{3/2}$ at 932.62 eV, Au $4f_{7/2}$ at 83.96 eV (Seah et al., 1998). O1s (α-Fe_3O_4) at 530.0 eV or O1s (OH) at 531.2 eV were used as charge reference for the analysed samples (Moulder et al., 1995). Error of binding energies of elemental lines is estimated to ± 0.2 eV. Samples were moved without air contact from the anoxic glovebox into the XP spectrometer by means of a transfer vessel (ULVAC-PHI Inc.). Data analysis was performed using ULVAC-PHI MultiPak program, version 9.9.

XPS analysis enabled the determination of the Fe(II)/Fe$_{total}$ ratio at the mineral surface. This evaluation method is described in Huber et al. (2012) and is based on a comparison between the Fe $2p_{3/2}$ spectra of a sample and a freshly prepared magnetite reference. The information depth

(95% of signal) of the Fe $2p_{3/2}$ elemental line is 2.2 nm for magnetite and 2.8 nm for maghemite, calculated by the CS2 equation of Cumpson and Seah (1997) taking in account a photoelectron take-off angle of 45°.

2.8 XAFS

For X-ray Absorption Near-Edge Structure (XANES) and Extended X-ray Absorption Fine-Structure (EXAFS) analysis at Rossendorf Beamline (ROBL) at ESRF, a 13 element high-purity germanium detector (Canberra) with digital signal processing (XIA) for fluorescence detection was used. The monochromator energy was calibrated with a gold foil (K-edge at 11,919 eV) because of its greater inertness and hence reliability in comparison to elemental Se. During the sample preparation, small amounts of Se-bearing magnetite powders were placed in sample holders and sealed with Kapton® tape. Spectra were collected at 15 K using a closed cycle He cryostat with a large fluorescence exit window and a low vibration level (CryoVac) in order to avoid photon-induced redox reactions.

The evaluation of the XAFS data, including dead time correction of the fluorescence signal, energy calibration and the averaging of single scans were performed with the software package SixPack (www.sams-xrays.com/sixpack). Normalization, transformation from energy into k space, and subtraction of a spline background was performed with WinXAS using routine procedures (Ressler, 1998).

3 Results

3.1 Magnetite adsorption capacity for selenite and selenate depending on pH
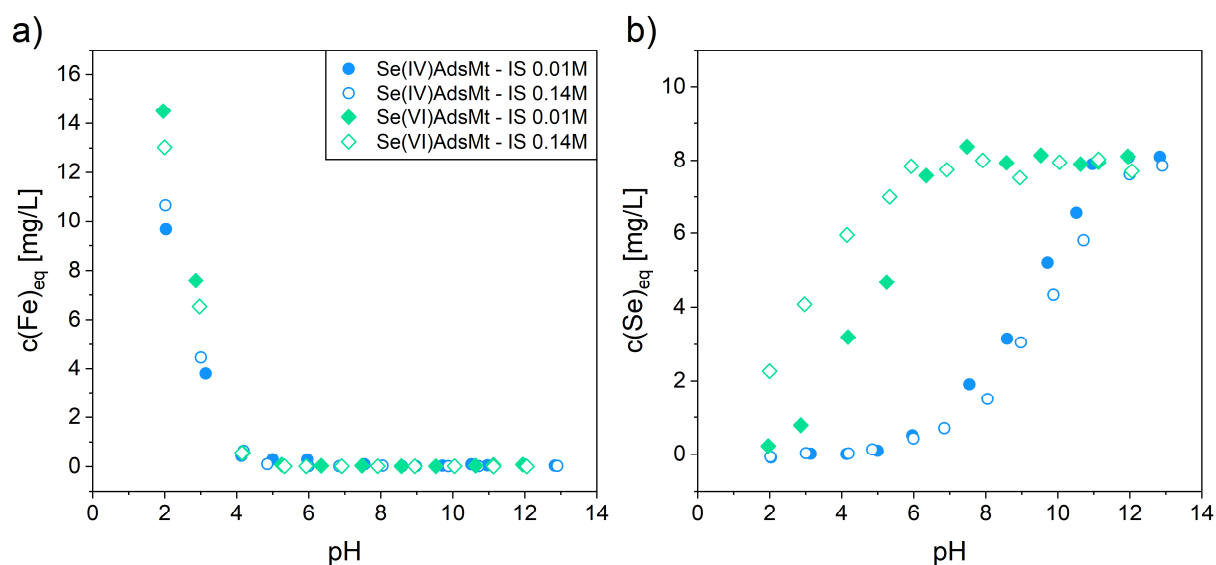
Figure S3. Residual (a) Fe and (b) Se concentrations after selenite or selenate adsorption on partially oxidized magnetite as a function of the solution pH; $c(Se)_0 = 10^{-4}$ mol/L ≈ 8 mg/L, Ionic strength (IS) = 0.01 or 0.14 mol/L KCl.

5

3.2 Characterisation of magnetite samples from selenite and selenate adsorption studies by solids analyses

To investigate the effects of selenite or selenate adsorption on the properties of the magnetite phase, selected samples from adsorption experiments were also characterized by various solids analysis methods. Table S1 shows the main hydrochemical data of four adsorption experiments together with results from solids analysis. The investigated samples came from selenite or selenate adsorption experiments, which were conducted at initial concentrations of 10^{-3} mol/L or 5×10^{-3} mol/L.

Table S2: Equilibrium concentrations of Fe and Se, Se removal (in % and log K_d) and mineral composition (Mt: magnetite) of selected samples with different initial Se amounts; "X"$c(Se)_0$ = "X" × 10^{-3} mol/L.

#	Se speciation	Sample	Mineral [a]	Se [b] [ppm]	pH [c]	$c(Fe)_{eq}$ [mol/L]	$c(Se)_0$ [mol/L]	$c(Se)_{eq}$ [mol/L]	Se sorbed [%]	q [mol/m²]	log K_d [L/kg]
1	-	Mt (initial) [d]	Mt	bdl	8.9	7.96E-07	-	-	-	-	-
2	Se(IV)	Se(IV)AdsMt[1]	Mt	2900	9.2	4.63E-06	1.00E-03	8.49E-04	15.4	1.42E-06	1.73
3	Se(IV)	Se(IV)AdsMt[5]	Mt	4200	9.2	bdl	5.02E-03	4.70E-03	6.4	2.93E-06	1.30
4	Se(VI)	Se(VI)AdsMt[1]	Mt	730	9.1	bdl	1.02E-03	1.01E-03	1.1	1.01E-07	0.50
5	Se(VI)	Se(VI)AdsMt[5]	Mt	120	9.1	bdl	5.11E-03	4.98E-03	2.6	1.24E-06	0.90

[a] Mineral composition (by XRD). [b] Se content of the solid phase (by EDXRF). [c] final pH after experiment. [d] Mt after synthesis

EDXRF data are in line with the results of the calculated Se uptake by hydrochemical data. They show that interaction with selenite causes higher absolute Se shares than selenate, although the total Se content of all analysed samples is overall very low. Even at relatively high initial selenite concentrations of 5×10^{-3} mol/L, the maximum Se content only amounted to approx. 0.42 wt.% in the corresponding sample.

XRD analysis furthermore demonstrated that the mineralogical composition of the initial magnetite phase was not affected by the adsorption of selenite or selenate respectively. XRD plots are all identical and no changes of the original magnetite peaks are discernible (Figure S4).
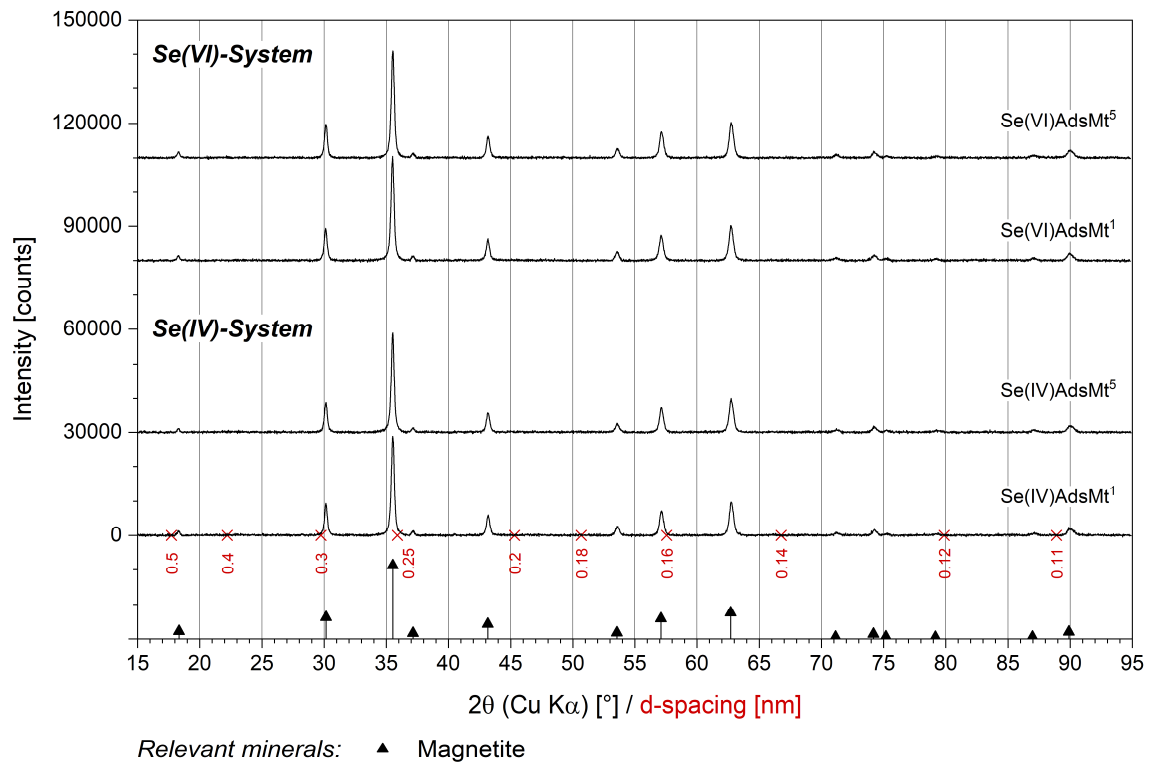
Figure S4. XRD results of magnetite samples from selenite and selenate adsorption studies. Initial Se concentrations: $^{"X"}c(Se)_0 =$ **"X"** $\cdot$ 10^{-3} **mol/L.**

Besides XRD analysis, solid samples from each Se system - selenite or selenate - were also characterised by SEM/EDX. SEM images of two samples together with their corresponding EDX analysis are shown in Figure S5. The comparison of both images with the initial magnetite phase after synthesis (see Börsig et al., 2018) indicates that neither adsorption of selenate nor selenite has an influence on the morphology of the solid phase. All samples consisted only of aggregated magnetite particles with a size of about 50 nm. Indications for the presence of additional mineral phases could not be found. However, it must be noted that due to the limited adsorption capacity of magnetite at pH 9.2, which results in low total Se contents, it is questionable whether mineralogical changes could be identified by XRD or SEM analysis.
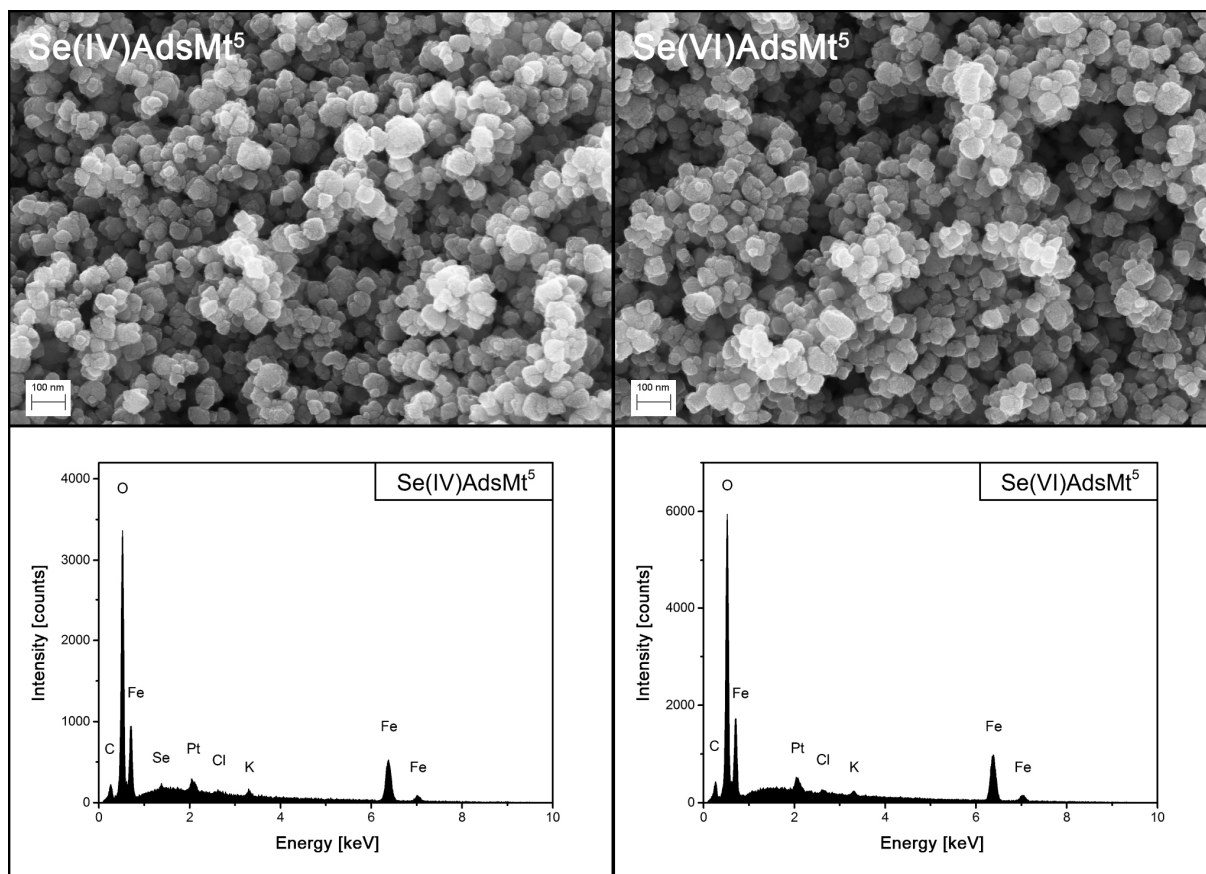
Figure S5. SEM/EDX results of magnetite samples from selenite and selenate adsorption studies; $c(Se)_0 = 5 \times 10^{-3}$ mol/L. EDX spectra shows the result of bulk analysis.

In order to gain more information about the chemical composition, the samples were also characterised by XPS (Table S2). XPS results confirmed the previous finding according to which the adsorption samples hardly differ from the original, Se-free magnetite. Like the original magnetite, the near-surface region of the unwashed adsorption samples mainly consists of Fe and O together with smaller amounts of C, Cl, K, and Na. The latter points to adsorption of dissolved ionic species such as Cl^- or HCO_3^- or their precipitation as salts. Regarding the $Fe(II)/Fe_{total}$ ratio of these samples, with values of 0.10–0.11 (± 5%), the remaining Fe(II) content after adsorption is only slightly lower than for the magnetite phase directly after synthesis (0.14). This illustrates that despite the constant oxic conditions during the adsorption process, the oxidation of magnetite into maghemite, which already occurred shortly after the magnetite synthesis, is not progressing significantly. The maghemite formed in the near-surface region of the particles, which already occurred shortly after the mineral synthesis, thus, seems to act as a passivating layer that prevents the magnetite from further aerial oxidation. Such a process was also described in previous studies on magnetite oxidation (He and Traina, 2005; Khan et al., 2015; Rebodos and Vikesland, 2010).

Like the SEM/EDX analysis, XPS data furthermore proved that the solid sample from the selenite system contained small amounts of Se (~0.8 at% Se at initial selenite concentrations of 5×10^{-3} mol/L). By analysing the binding energies of its spectral lines, the oxidation state of this Se proportion was identified as Se(IV). This demonstrates that the Se retention mechanism is not accompanied by a change of the Se oxidation state. Due to the low uptake at pH 9.2, the sample of the selenate system on the other hand contained too little Se to be analysed via XPS.

Table S3. **XPS results of magnetite samples from selenite and selenate adsorption studies as well as pure magnetite reference (all unwashed): Atomic concentrations (at%) of main elements; Binding energies in eV. "X" c(Se)$_0$ = "X"·10^{-3} mol/L; # pure magnetite from Börsig et al. (2018).**

Sample	C	N	O	Na	Cl	K	Fe	Se	Fe(II)/Fe$_{tot}$ [%]
Magnetite (pure)[#]	9.5	0.6	53.1	1.3	0.7	3.0	31.8	---	13.8
Se(IV)AdsMt[5]	5.5	0.9	54.8	0.3	0.6	2.4	34.8	0.8	11.2
Se(VI)AdsMt[5]	9.0	0.4	54.5	---	0.8	2.0	33.3	---	9.5

Atomic concentrations [at%]: relative error ± 10-20%. Fe(II)/Fe$_{tot}$: relative error ± 5%.

Sample	Se 3s	Se L$_3$M$_{45}$M$_{45}$	Se 3p$_{3/2}$	Se L$_2$M$_{45}$M$_{45}$	O 1s	*(charge ref.)*	Se valency
Se(IV)AdsMt[5]	233.9	185.6	164.9	144.1	530.0	Fe$_3$O$_4$	Se(IV)

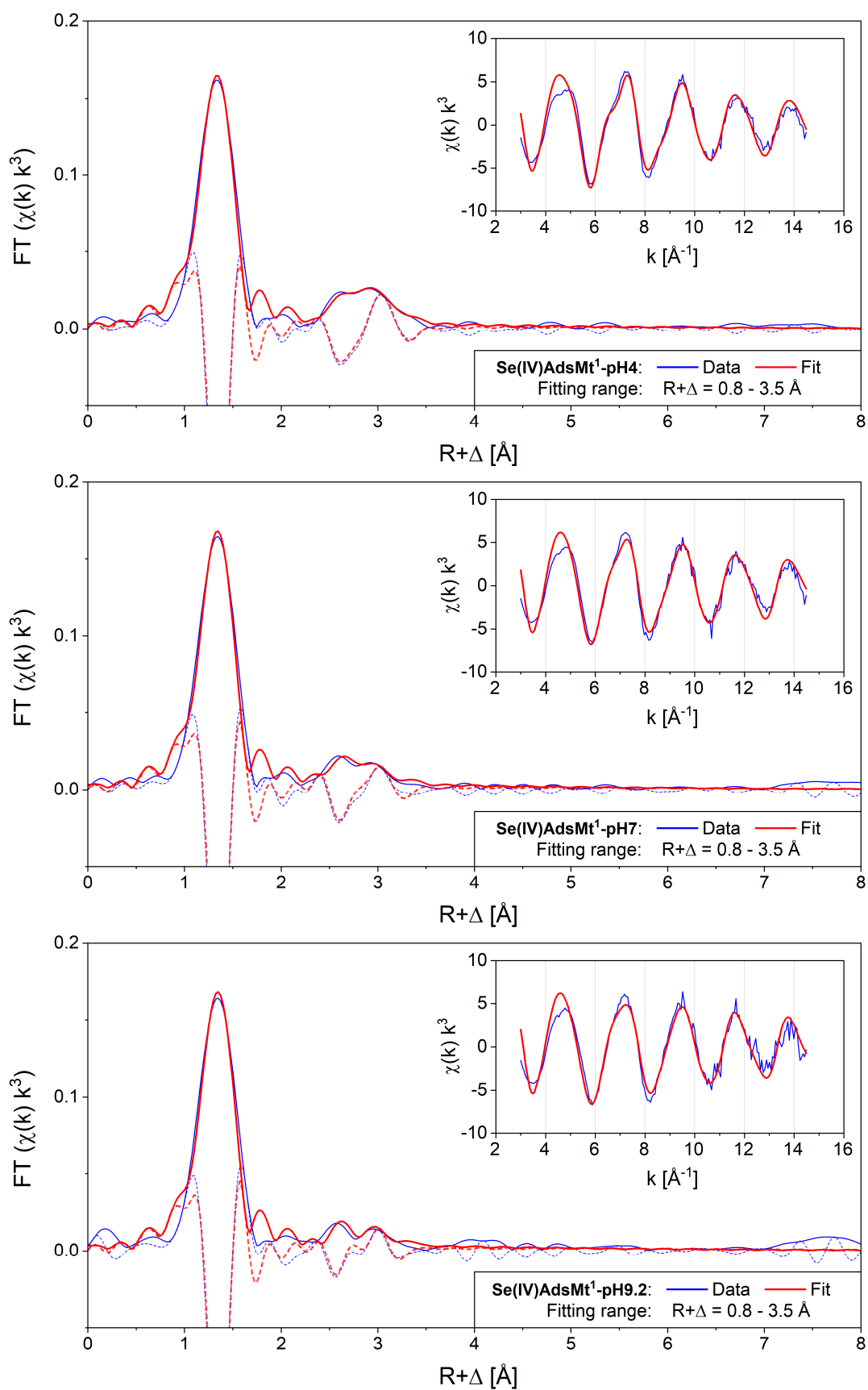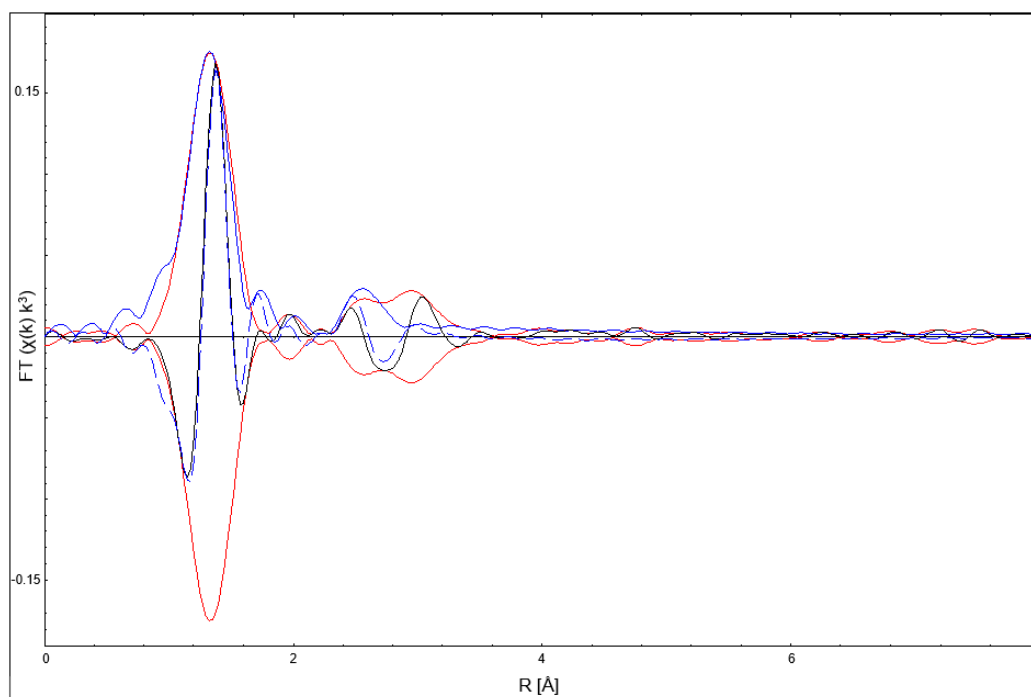Binding energy [eV]: error ± 0.2 eV

3.3 EXAFS fit results

Figure S6. Se-K edge EXAFS fit results of selenite-magnetite adsorption studies performed at different pH values; $c(Se)_0 = 10^{-3}$ mol/L.

Figure S7. Example of an unsatisfactory EXAFS fit using only one Se-Fe shell for fitting the FT peaks in the range 2.3–3.5 Å.

References

Börsig, N., Scheinost, A.C., Shaw, S., Schild, D., Neumann, T., 2018. Retention and multiphase transformation of selenium oxyanions during the formation of magnetite via iron(II) hydroxide and green rust. Dalt. Trans. 47, 11002–11015.

Cumpson, P.J., Seah, M.P., 1997. Elastic Scattering Corrections in AES and XPS. II. Estimating Attenuation Lengths and Conditions Required for their Valid Use in Overlayer/Substrate Experiments. Surf. Interface Anal. 25, 430–446.

He, Y.T., Traina, S.J., 2005. Cr(VI) reduction and immobilization by magnetite under alkaline pH conditions: The role of passivation. Environ. Sci. Technol. 39, 4499–4504.

Huber, F., Schild, D., Vitova, T., Rothe, J., Kirsch, R., Schäfer, T., 2012. U(VI) removal kinetics in presence of synthetic magnetite nanoparticles. Geochim. Cosmochim. Acta 96, 154–173.

Khan, U.S., Amanullah, Manan, A., Khan, N., Mahmood, A., Rahim, A., 2015. Transformation mechanism of magnetite nanoparticles. Mater. Sci. Pol. 33, 278–285.

Moulder, J.F., Stickle, W.F., Sobol, P.E., Bomben, K.D., 1995. Handbook of X-ray Photoelectron Spectroscopy. ULVAC-PHI, Inc. (Japan); Physical Electronics USA, Inc.

Rebodos, R.L., Vikesland, P.J., 2010. Effects of oxidation on the magnetization of nanoparticulate magnetite. Langmuir 26, 16745–16753.

Ressler, T., 1998. WinXAS: A program for X-ray absorption spectroscopy data analysis under MS-Windows. J. Synchrotron Radiat. 5, 118–122.

Salah, S., Wang, L., 2014. Speciation and solubility calculations for waste relevant radionuclides in Boom Clay. External Report of the Belgian Nuclear Research Centre. SCK•CEN-ER-198, Mol, BEL.

Seah, M.P., Gilmore, I.S., Beamson, G., 1998. XPS: Binding Energy Calibration of Electron Spectrometers 5 - Re-evaluation of the Reference Energies. Surf. Interface Anal. 26, 642–649.

Séby, F., Potin-Gautier, M., Giffaut, E., Borge, G., Donard, O.F.X., 2001. A critical review of thermodynamic data for selenium species at 25°C. Chem. Geol. 171, 173–194.